AN EXTENDED MECHANICAL THRESHOLD STRESS PLASTICITY MODEL. I. MODELING 6061-T6 ALUMINUM ALLOY

BISWAJIT BANERJEE AND ANUP S. BHAWALKAR

ABSTRACT. The mechanical threshold stress plasticity model of Follansbee and Kocks was designed to predict the flow stress of metals and alloys in the regime where thermally activated mechanisms are dominant and high temperature diffusion effects are negligible. In this paper we present a model that extends the original mechanical threshold stress to the high strain-rate regime (strain rates higher than 10^4 s^{-1}) and attempts to allow for high temperature effects. We use a phonon drag model for moderate strain rates and an overdriven shock model for extremely high strain rates. A temperature dependent model for the evolution of dislocation density is also presented. In addition, we present a thermodynamically-based model for the evolution of temperature with plastic strain. Parameters for 6061-T6 aluminum alloy are determined and compared with experimental data. The strain-rate dependence of the flow stress of 6061-T6 aluminum is found to be in excellent agreement with experimental data. The amount of thermal softening is underestimated at high temperatures (greater than 500 K) but still is an improvement over the original model. We also find that the pressure dependence of the shear modulus does not completely explain the pressure dependence of the flow stress of 6061-T6 aluminum alloy.

1. INTRODUCTION

With the advent of powerful computational machines and algorithms, it is now possible to simulate of processes such as accidental impact of vehicles, high-speed machining, high- and hyper-velocity impact and penetration, and explosive forming. These processes typically involve plastic deformations at high strain rates (10^2 s^{-1} to 10^9 s^{-1}) and often temperatures greater than $0.6 \, T_m$ (T_m is the melting temperature of the material). Adiabatic shear banding often accompanies the process and provides zones where fractures nucleate. A crucial component in the numerical modeling of plastic deformations under these conditions is a model that describes the evolution of the flow stress under a large range of strain-rates and temperatures.

The mechanical threshold stress (MTS) flow stress model [1, 2, 3] was originally developed with two assumptions:

(1) Thermally activated dislocation motion was dominant and viscous drag effects on dislocation motion were small. This assumption essentially restricts the model to strain rates of 10^4 s^{-1} and less.

(2) High temperature diffusion effects (such as solute diffusion from inside the grains to grain boundaries) were absent. This assumption limits the range of applicability of the model to temperatures less than around $0.6 \, T_m$ (depending on the material). For 6061-T6 aluminum alloy this temperature is approximately 450 - 500 K.

The aluminum alloy 6061 is composed of 97.5% aluminum, 1.0 % magnesium, 0.6 % silicon, 0.34 % iron, 0.3 % copper, 0.2 % chromium, and around 0.04 % zinc and titanium by weight. The T6 hardening treatment varies by manufacturer but usually involves a solution treatment at 810 K followed by

quenching in water and then aging for a few hours at around 450 K. The solution treatment leads to a homogeneous supersaturated solid solution. The quenching step is performed to take the supersaturated solution to a two-phase region of the phase diagram. In the aging step, the magnesium silicide (Mg_2 Si) phase is precipitated in such a way that the precipitate is evenly distributed inside the grains. There is also some precipitation of AlFeSi at the grain boundaries. The precipitates inside the grains impede dislocation motion and make the alloy harder. The lightness, strength, weldability, and corrosion resistance of the 6061-T6 alloy makes it ideal for heavy duty structures in marine applications (among other uses). However, at about 550K, the alloying Mg_2 Si precipitates start to diffuse toward the grain boundaries and accumulate at the grain boundaries. As a result, 6061-T6 aluminum softens considerably at high temperatures. More detail about the processes involved can be found in [4].

Simulations of high velocity sphere-cylinder impact experiments using a MTS model for an aluminum alloy containing 1% magnesium [5] showed that the model underestimated the flow stress at strain rates greater than 10^5 s^{-1}. Also, high temperature Taylor impact simulations using the same model showed that the flow stress was significantly overestimated for temperatures greater than 450 K [6].

In this paper, we extend the MTS model so that it can be used for strain rates greater than 10^4 s^{-1} and for temperatures greater than 450 K. To extend the model to the regime of high strain rates, we incorporate a model for viscous drag controlled dislocation motion (which becomes dominant at strain rates greater than 10^4 s^{-1}). In addition, we incorporate a model for the overdriven shock regime (strain-rates greater than 10^9 s^{-1}). To account for the effect of thermally assisted diffusion of solutes, we incorporate an empirical modification of the original model for thermally activated mechanisms.

The evolution of temperature with plastic strain can be quite important in some situations (such as the development of adiabatic shear bands). We derive an expression for the Taylor-Quinney coefficient from thermodynamic principles and postulate a temperature dependent model for the evolution of this quantity.

The parameters of the extended MTS model are then fit using experimental stress-strain data for 6061-T6 aluminum from the literature wherever available. The flow stress estimated from the model is then compared with experimental data. Next, predictions of the model for a range of strain rates, temperatures, and levels of plastic strain are discussed. Finally, some concluding remarks are given and potential areas of future work are discussed.

2. The Extended Mechanical Threshold Stress Model

The original mechanical threshold stress (MTS) model [1, 2] for the flow stress (σ_y) can be written as

$$\sigma_y(\sigma_e, \dot{\varepsilon}, p, T) = [\tau_a + \tau_i(\dot{\varepsilon}, T) + \tau_e(\sigma_e, \dot{\varepsilon}, T)] \frac{\mu(p, T)}{\mu_0} \tag{1}$$

where σ_e is an evolving internal variable that has units of stress (also called the mechanical threshold stress), $\dot{\varepsilon}$ is the strain rate, p is the pressure, T is the temperature, τ_a is the athermal component of the flow stress, τ_i is the intrinsic component of the flow stress due to barriers to thermally activated dislocation motion, τ_e is the component of the flow stress due to structure evolution (e.g., strain hardening), μ is the shear modulus, and μ_0 is a reference shear modulus at 0 K and ambient pressure.

2.1. **Athermal component.** The athermal component of the yield stress is a function of grain size, dislocation density, distribution of solute atoms, and other long range barriers to dislocation motion. This component may either be constant or may evolve with deformation. A simple model for this component can be written as [7, 8]:

$$\tau_a = \tau_0 + \frac{k}{\sqrt{d}} \tag{2}$$

where τ_0 is the component due to far field dislocation interactions and the second term represents contribution due to the Hall-Petch effect where k is a material constant and d is the grain size.

2.2. **Intrinsic component.** In the MTS model, the intrinsic component of the flow stress is assumed to be dependent only on thermally activated mechanisms in the absence of solute diffusion. This component can be expressed in the phenomenological Arrhenius form given below (see [9] Section 44 for an explanation)

$$\tau_i = S_i\,\sigma_i\;;\qquad S_i := \left[1 - \left(\frac{k_b\,T}{g_{0i}\,b^3\,\mu(p,T)}\ln\frac{\dot{\varepsilon}_{0i}}{\dot{\varepsilon}}\right)^{1/q_i}\right]^{1/p_i} \tag{3}$$

where σ_i is the intrinsic component of the mechanical threshold stress (flow stress at 0 K), k_b is the Boltzmann constant, b is the magnitude of Burgers vector, g_{0i} is a normalized activation energy, $\dot{\varepsilon}_{0i}$ is a constant reference strain rate, and p_i, q_i are constants. The constant p_i can take values between 0 and 1, while q_i can take values between 1 and 2.

In order to fit the high temperature data for 6061-T6 aluminum better, we have found that a better relation for τ_i has the form

$$\tau_i = \sigma_i\left[1 - \left\{\left(\frac{k_b\,T}{g_{0i}\,b^3\,\mu(p,T)}\ln\frac{\dot{\varepsilon}_{0i}}{\dot{\varepsilon}}\right)^{1/q_i}\right\}^2\right]^{1/p_i}. \tag{4}$$

This relation is equivalent to using values of q_i between 0.5 and 1. If we use such a value in the original MTS model, the value of τ_i tends to become constant as the strain rate is increased. Recall that the original MTS model does not account for the effect of viscous drag at high strain rates and the model predicts only a small increase in the flow stress with strain rate if q_i is between 1 and 2. The small reduction in the flow stress at high strain rates due to a value of q_i between 0.5 and 1 is easily offset by incorporating a simple model for viscous drag into the MTS model.

2.3. **Viscous drag component.** To incorporate viscous drag effects due to phonon damping, forest dislocations, and solute atoms, we add a term to the equation for τ_i of the form [10, 11]

$$\tau_v = \frac{2}{\sqrt{3}}\frac{B}{\rho_m\,b^2}\dot{\varepsilon} \tag{5}$$

where B is the drag coefficient, ρ_m is the mobile dislocation density, and b is the magnitude of the Burgers vector. We assume that a good estimate of the value of the drag coefficient can be obtained if we consider only damping due to phonon scattering [12]. However, at low temperatures (< 50 K), electron damping can dominate and a model for that should be used in addition to phonon damping (for more details see [13] p. 251-260).

The viscous drag coefficient can be written as [14]

$$B \approx \lambda_p\,B_p = \frac{\lambda_p\,k_b\,T\,\omega_D^2}{\pi^2\,\bar{c}^3} \tag{6}$$

where B_p is the phonon drag coefficient, $\lambda_p \geq 1$ is a correction factor, ω_D is the Debye frequency and $\bar{c}$ is the average sound speed. The Debye frequency is given by

$$\omega_D = \frac{2\pi\,k_b\,\theta_D}{h} = 2\,\pi\,\bar{c}\left(\frac{3\,\rho}{4\,\pi\,M}\right)^{1/3} = \left(\frac{6\,\pi^2\,\rho}{M}\right)^{1/3}\bar{c} \tag{7}$$

where θ_D is the Debye temperature, h is Planck's constant, and M is the atomic mass. The average sound speed is defined as

$$\frac{1}{\bar{c}^3} = \frac{1}{3}\left(\frac{2}{c_s^3} + \frac{1}{c_l^3}\right) \; ; \; c_s = \sqrt{\frac{\mu}{\rho}} \; ; \; c_l = \sqrt{\frac{2\mu(1-\nu)}{\rho(1-2\nu)}} \tag{8}$$

where c_s is the transverse sound speed, c_l is the longitudinal sound speed, and ν is the Poisson's ratio. Assuming that the Poisson's ratio is 1/3, we can get an approximation for $\bar{c}$ in terms of the shear sound speed as

$$\bar{c} \approx \left(\frac{24}{17}\right)^{1/3} c_s \; . \tag{9}$$

Alternatively, we can use Liebfried's model [10, 15, 16, 12] for scattering of phonons by dislocations

$$B \approx \lambda_p \, B_p = \frac{\lambda_p \, q}{10 \, c_s} \langle E \rangle \tag{10}$$

where λ_p is a correction factor, q is the cross-section of the dislocation core per unit length and $\langle E \rangle$ is the average internal energy density. From Debye theory, we have

$$\langle E \rangle = \frac{3 \, k_b \, T \, \rho}{M} \, D_3\left(\frac{\theta_D}{T}\right) \; ; \; \theta_D = \frac{h \, \bar{c}}{k_b}\left(\frac{3 \, \rho}{4 \, \pi \, M}\right)^{1/3} \tag{11}$$

where the Debye function D_3 is defined as

$$D_3(x) := \frac{3}{x^3} \int_0^x \frac{z^3}{\exp(z) - 1} \, dz \; . \tag{12}$$

Note that the component of the flow stress due to viscous drag is both temperature and pressure dependent. A closed form expression can be obtained for the Debye integral in terms of polylogarithms (see for example [17]). However, there is a singularity at $z = 0$ and analytic continuation methods are needed to evaluate the polylogarithms for values of $z > 0$. Alternatively, expansions in terms of Chebyshev polynomials [18, 19] may be used. For computational purposes, a look-up table of values (for example [20]) is the most efficient.

The second variable that is needed to compute τ_v is the density of mobile dislocations (ρ_m). The density of mobile dislocations depends on the prior strain history of a material and also on the strain, the temperature, and the strain rate. A simple model for the evolution of mobile dislocations as a function of plastic strain can be written as [21, 22]

$$\begin{aligned}\frac{\mathrm{d}\rho_m}{\mathrm{d}\varepsilon_p} &= \frac{M_1}{b^2}\left(\frac{\rho_f}{\rho_m}\right) - I_2(\dot{\varepsilon}, T) \, \rho_m - \frac{I_3}{b} \, \sqrt{\rho_f} \\ \frac{\mathrm{d}\rho_f}{\mathrm{d}\varepsilon_p} &= I_2(\dot{\varepsilon}, T) \, \rho_m + \frac{I_3}{b} \, \sqrt{\rho_f} - A_4(\dot{\varepsilon}, T) \, \rho_f\end{aligned} \tag{13}$$

where ρ_f is the density of forest dislocations, b is the magnitude of the Burgers' vector, M_1 is a rate of mobilization of dislocations, I_2 is a rate of immobilization of mobile dislocations due to interactions between mobile dislocations, I_3 is another immobilization rate due to interactions with forest dislocations, and A_4 is the rate of annihilation of forest dislocations due to climb, cross-slip, or diffusion.

To solve the system of differential equations (13), we need initial values of ρ_m and ρ_f. We may also assume that the density of forest dislocations saturates at a value of ρ_{fs}, that is, $\mathrm{d}\rho_f/\mathrm{d}\varepsilon_p = 0$ at $\rho_f = \rho_{fs}$.

Since the density of forest dislocations is easier to measure than the rate of annihilation A_4, we use ρ_{fs} to obtain the following expression for A_4:

$$A_4(\dot{\varepsilon}, T) = I_2(\dot{\varepsilon}, T) \, \frac{\rho_m}{\rho_{fs}} + \frac{I_3}{b} \frac{1}{\sqrt{\rho_{fs}}} \, . \tag{14}$$

The rate I_2 and the saturation value ρ_{fs} are, in general, temperature and strain-rate dependent. We assume that the strain rate dependence of these quantities is negligible for aluminum alloys and only consider temperature dependence. Based on the experimental observation that the temperature dependence of the flow stress of aluminum alloys follows a sigmoidal curve [23], we assume that I_2 and ρ_{fs} have the following temperature dependence:

$$
\begin{aligned}
I_2(T) &= I_{20} \left(\frac{\alpha_I}{1 + \exp[-\beta_I \, (1 - 2\,\widehat{T})]} \right) \\
\rho_{fs}(T) &= \rho_{fs0} \left(1 - \frac{\alpha_f}{1 + \exp[\beta_f \, (1 - 2\,\widehat{T})]} \right)
\end{aligned}
\tag{15}
$$

where I_{20} is the value of I_2 at 0 K, ρ_{fs0} is the value of ρ_{fs} at 0 K, $\widehat{T} = T/T_m$ where T_m is the melting temperature, α_I, α_f are scaling factors, and β_I, β_f are constants that have values greater than 3.

2.4. **Structure evolution component.** The evolution of dislocation density could be used to determine the component of the flow stress that depends on the evolution of the structure of a material (see for instance [22]). However, equations 13 form a stiff system of differential equations and are not ideal for numerical simulations, particularly explicit calculations needed for high rate processes. Instead, we use the approach originally suggested by Follansbee and Kocks [1] and describe the component of the flow stress due to structure evolution by

$$\tau_e(\sigma_e, \dot{\varepsilon}, T) = S_e \, \sigma_e \, ; \qquad S_e := \left[1 - \left(\frac{k_b \, T}{g_{0e} \, b^3 \, \mu(p, T)} \ln \frac{\dot{\varepsilon}_{0e}}{\dot{\varepsilon}} \right)^{1/q_e} \right]^{1/p_e} \tag{16}$$

where σ_e is an internal variable (the structure evolution component of the mechanical threshold stress) that evolves with the deformation, g_{0e} is a normalized activation energy, $\dot{\varepsilon}_{0e}$ is a reference strain rate, and p_e, q_e are constants.

The evolution of σ_e is assumed to be governed by the modified Voce rule

$$\frac{\mathrm{d}\sigma_e}{\mathrm{d}\varepsilon_p} = \theta_0 \left[1 - \left(\frac{\sigma_e}{\sigma_{es}} \right)^2 \right] \tag{17}$$

where θ_0 is the initial hardening modulus and σ_{es} is the saturation value of σ_e. This equation can be solved in closed form along a constant temperature and strain-rate path to get

$$\sigma_e(\varepsilon_p) = \sigma_{es} \left[\frac{A_\sigma \, \exp(\beta) + 1}{A_\sigma \, \exp(\beta) - 1} \right] \, ; \; A_\sigma := \frac{\sigma_{ei} + \sigma_{es}}{\sigma_{ei} - \sigma_{es}} \, ; \; \beta := \frac{2 \, \theta_0 \, \varepsilon_p}{\sigma_{es}} \tag{18}$$

where σ_{ei} is the value of σ_e at zero plastic strain and can be non-zero depending on the prior strain history of the material. For the special case where σ_{ei} is zero, we have

$$\sigma_e(\varepsilon_p) = \sigma_{es} \left[\frac{\exp(\beta) - 1}{\exp(\beta) + 1} \right] \, . \tag{19}$$

The initial hardening modulus is assumed to be given by a relation of the form

$$\theta_0 = \mu(p,T) \left[a_0 + a_1 \, \ln\left(\frac{\dot{\varepsilon}_\theta}{\dot{\varepsilon}}\right) + a_2 \, \widehat{T} + a_3 \, \widehat{T} \, \ln\left(\frac{\dot{\varepsilon}_\theta}{\dot{\varepsilon}}\right) \right] \tag{20}$$

where a_0, a_1, a_2, a_3 are constants and $\dot{\varepsilon}_\theta$ is a reference strain rate, and $\widehat{T} = T/T_m$ where T_m is the melting temperature. The value of θ_0 is not allowed to be negative.

The saturation value of structure evolution stress is computed using an Arrhenius type relation of the form

$$\ln\left(\frac{\sigma_{es}}{\sigma_{0es}}\right) = \left(\frac{k_b \, T}{g_{0es} \, b^3 \, \mu(\rho,T)}\right) \ln\left(\frac{\dot{\varepsilon}}{\dot{\varepsilon}_{0es}}\right) \tag{21}$$

where σ_{0es} is the saturation threshold stress for deformation at 0 K, g_{0es} is a normalized activation energy, and $\dot{\varepsilon}_{0es}$ is a reference strain rate.

2.5. **Overdriven shock regime.** At strain-rates between 10^9 s^{-1} and 10^{12} s^{-1}, the plastic wave over-runs the elastic precursor and produces a steeper shock front than is attainable due to adiabatic elastic compression. Such a shock is called "overdriven". In order to allow for overdriven shocks in our model, we follow the approach used in the Preston-Tonks-Wallace model [24]. The flow stress under overdriven shock conditions (and assuming J_2 plasticity) is given by

$$\sigma_{ys} = \sigma_{ys0} + y_1 \left(\frac{\dot{\varepsilon}}{\gamma \, \dot{\xi}}\right)^{y_2} \mu(p,T) \tag{22}$$

where σ_{ys0} is a lower limit on the flow stress, y_1, y_2 are material parameters, γ is a scaling factor, and $\dot{\xi}$ is a reference strain rate. The reference strain rate is defined as

$$\dot{\xi} := \frac{1}{2} \left(\frac{4 \, \pi \, \rho}{3 \, M}\right)^{1/3} c_s \tag{23}$$

where M is the atomic mass and c_s is transverse sound speed. We assume that there is no hardening in the overdriven shock regime.

2.6. **Behavior after melting.** After the temperature crosses the melting temperature (T_m), we have to model the material as a liquid. Though, strictly speaking, the behavior of an aluminum alloy melt is non-Newtonian, we use a Newtonian model of the following form to determine the deviatoric stress in the material after it has melted:

$$\sigma_y = \mu_v \, \dot{\varepsilon} \tag{24}$$

where μ_v is the shear viscosity of the melt. The shear viscosity of aluminum alloys can be estimated by first computing the viscosities of the constituent elements using the Andrade equation [25, 26] (alternative approaches can be found in [27, 28]). The viscosity of the alloy can then be calculated using the Moelwyn-Hughes model for binary alloys [29, 28]. However, since we are not interested in the details of the motion of the melt, we simplify our model by using a constant value of $\mu_v = 2.0 \times 10^{-4}$ Pa-s in our calculations.

2.7. **The extended flow stress model.** The final expression for the flow stress is

$$\sigma_y = \begin{cases} \min\left\{ \left[\tau_v + (\tau_a + \tau_i + \tau_e)\dfrac{\mu}{\mu_0}\right] , \sigma_{ys} \right\} & \text{for } T < T_m \\ \mu_v \, \dot{\varepsilon} & \text{for } T \geq T_m \end{cases} \tag{25}$$

2.8. **Shear modulus, melting temperature, EOS, specific heat.** To complete the model, we need an expression for the shear modulus as a function of temperature and pressure. We have used a modified form of the Nadal-LePoac model [30] in which the pressure dependence of the shear modulus is determined by the generalized Guinan-Steinberg formula ([31, 32]) :

$$\mu(p,T) = \frac{1}{\mathcal{J}(\widehat{T},\zeta)} \left[\left\{ \mu_0 + p \, \frac{\partial \mu}{\partial p} \left(\frac{a_1}{\eta^{1/3}} + \frac{a_2}{\eta^{2/3}} + \frac{a_3}{\eta} \right) \right\} (1 - \widehat{T}) + \frac{\rho}{C \, M} \, k_b \, T \right]$$

$$\eta := \frac{\rho}{\rho_0} \; ; \; C := \frac{(6\pi^2)^{2/3}}{3} f^2 \tag{26}$$

where $\mathcal{J}$ is a scaling factor that allows for smooth transition of the shear modulus to melt, $\widehat{T} := T/T_m$, T_m is the melting temperature, ζ is a material parameter, μ_0 is the shear modulus at 0 K and ambient pressure, $\partial \mu / \partial p$ is the slope of the shear modulus versus pressure curve at 0 K, a_1, a_2, a_3 are material constants, ρ_0 is the mass density in the initial state, M is the atomic mass, f is the Lindemann constant, and

$$\mathcal{J}(\widehat{T},\zeta) := 1 + \exp\left[-\frac{1 + 1/\zeta}{1 + \zeta/(1 - \widehat{T})} \right] \quad \text{for} \quad \widehat{T} \in [0, 1 + \zeta] \, . \tag{27}$$

For situations where $\rho/\rho_0 < 0.95$ (high hydrostatic tension), we set the shear modulus to be equation to the value obtained for $\rho/\rho_0 = 0.95$.

We use the Burakovsky-Greeff-Preston (BGP) model [33] to determine the melting temperature. This model improves upon the widely used Steinberg-Cochran-Guinan model [34] which is also based on the Lindemann criterion. In the BGP model, the Grüneisen gamma is modeled as

$$\Gamma(\rho) = \frac{1}{2} + \frac{\Gamma_1}{\rho^{1/3}} + \frac{\Gamma_2}{\rho^q} \tag{28}$$

where Γ_1, Γ_2, q are material constants and $q > 1$. This form of $\Gamma(\rho)$ leads to the following expression for the melting temperature as a function of density:

$$T_m(\rho) = T_{m0} \, \eta^{1/3} \, \exp\left\{ 6\Gamma_1 \left(\frac{1}{\rho_0^{1/3}} - \frac{1}{\rho^{1/3}} \right) + \frac{2\Gamma_2}{q} \left(\frac{1}{\rho_0^q} - \frac{1}{\rho^q} \right) \right\} \; ; \; \eta := \frac{\rho}{\rho_0} \tag{29}$$

where T_{m0} is the melt temperature when $\rho = \rho_0$.

The pressure is calculated using the Holzapfel equation of state [35, 36, 31] which has the form

$$p(\rho) = 3 \, B_0 \left[\eta^{5/3} - \eta^{4/3} \right] \exp\left\{ 1.5 \, (B_0' - 3) \left[1 - \eta^{-1/3} \right] \right\} \; ; \; \eta := \frac{\rho}{\rho_0} \tag{30}$$

where B_0 is the bulk modulus at $p = 0$ and B_0' is the slope of the pressure-density curve at $p = 0$.

We use an empirical temperature-dependent specific heat model and ignore the difference between the values of specific heat at constant pressure and at constant volume. The specific heat model is of the form [37]

$$C_v = \begin{cases} A_1 + B_1 \, T + C_1 \, T^2 & \text{for } T < 273K \\ A_2 + B_2 \, T & \text{for } T \geq 273K \end{cases} \tag{31}$$

where A_1, A_2, B_1, B_2, C_1 are constants.

3. Evolution of temperature due to plastic dissipation

To determine the increase in temperature due to plastic dissipation, we first assume that the deformation gradient (F) can be split multiplicatively into elastic and plastic parts ($F = F_e \cdot F_p$). We also assume that there is no volume change during the plastic part of the deformation.

The elastic strain measure (E_e) (with respect to the intermediate configuration) and the plastic strain rate (d_p) are defined as (see [38] for details)

$$E_e := \frac{1}{2}[F_e^T \cdot F_e - 1] \; ; \; d_p := \frac{1}{2}[F_e \cdot \dot{F}_p \cdot F_p^{-1} \cdot F_e^{-1} + F_e^{-T} \cdot F_p^{-T} \cdot \dot{F}_p^T \cdot F_e^T] \tag{32}$$

The stress measure in the intermediate configuration (that is work conjugate to E_e) is given by the pull-back of the Cauchy stress by the elastic part of the deformation gradient:

$$\widetilde{S} = \frac{\rho_0}{\rho} F_e^{-1} \cdot \sigma \cdot F_e^{-T} . \tag{33}$$

Then the balance of energy can be expressed as

$$\rho \, T \, \dot{\eta} = -\boldsymbol{\nabla} \cdot \mathbf{q} + \rho \, r + \sigma : d_p - \frac{\rho}{\rho_0} \sum_{n=1}^N Q_n \, \dot{q}_n \tag{34}$$

where η is the entropy density, $\boldsymbol{\nabla} \cdot (\bullet)$ denotes the divergence (with respect to the current configuration), r is a internal heat source term, σ is the Cauchy stress, and q_n is a set of internal variables. The quantities Q_n are work conjugate to the internal variables q_n and are defined as

$$Q_n := -\rho_0 \, \frac{\partial g}{\partial q_n} \qquad \text{for } n = 1 \ldots N \tag{35}$$

where $g(\widetilde{S}, T, q_n)$ is the specific Gibbs free energy (per unit mass) and ρ_0 is the density in the intermediate configuration (here assumed to be the same as that in the reference configuration).

The internal variable in the MTS model is σ_e, that is

$$q_1 = \sigma_e \; ; \; Q_1 = -\rho_0 \, \frac{\partial g}{\partial \sigma_e} . \tag{36}$$

Under adiabatic conditions which occur for high strain-rate deformations, the heat flux and internal heat sources can be neglected. In that case, the energy equation takes the form

$$\rho \, T \, \dot{\eta} = \sigma : d_p + \rho \, \frac{\partial g}{\partial \sigma_e} \, \dot{\sigma}_e . \tag{37}$$

Assuming that the entropy can be derived from the specific Gibbs free energy, it can be shown, after some algebra, that [38]

$$\dot{\eta} = \frac{\partial \eta}{\partial \widetilde{S}} : \dot{\widetilde{S}} + \frac{\partial \eta}{\partial T} \dot{T} + \frac{\partial \eta}{\partial \sigma_e} \dot{\sigma}_e = \frac{1}{\rho_0} \frac{\partial E_e}{\partial T} : \dot{\widetilde{S}} + \frac{C_v}{T} \dot{T} - \frac{1}{\rho_0} \frac{\partial \widetilde{S}}{\partial T} : \dot{E}_e + \frac{\partial}{\partial T}\left(\frac{\partial g}{\partial \sigma_e}\right) \dot{\sigma}_e . \tag{38}$$

Substitution into the energy equation yields

$$\rho \, C_v \, \dot{T} = \sigma : d_p + \rho \left[\frac{\partial g}{\partial \sigma_e} - T \frac{\partial}{\partial T}\left(\frac{\partial g}{\partial \sigma_e}\right)\right] \dot{\sigma}_e . \tag{39}$$

It is conventional to use a factor χ (called the Taylor-Quinney coefficient) to relate the rate of change of temperature to the plastic work $\mathcal{P}_p := \sigma : d_p$ using the relation

$$\dot{T} = \frac{\chi \, \sigma : d_p}{\rho \, C_v} . \tag{40}$$

Therefore, from equation (39) we observe that

$$\chi = 1 - \left[T \frac{\partial}{\partial T} \left(\frac{\partial g}{\partial \sigma_e} \right) - \frac{\partial g}{\partial \sigma_e} \right] \left(\frac{\rho \, \dot{\sigma}_e}{\boldsymbol{\sigma} : \boldsymbol{d}_p} \right) . \tag{41}$$

Clearly χ evolves with σ_e and T and cannot be assumed to be around 0.9 as is usually the case. However, the functional form of the Gibbs free energy function is not obvious and we have to make certain assumptions to obtain a function that matches experimental observations (see for instance [39]).

If we make the assumption that $\boldsymbol{\sigma} : \boldsymbol{d}_p \approx \sigma_y \, \dot{\varepsilon}_p$, the expression in equation (41) reduces to

$$\chi = 1 - \left[T \frac{\partial}{\partial T} \left(\frac{\partial g}{\partial \sigma_e} \right) - \frac{\partial g}{\partial \sigma_e} \right] \left(\frac{\rho}{\sigma_y} \right) \frac{\mathrm{d}\sigma_e}{\mathrm{d}\varepsilon_p} . \tag{42}$$

Replacing the derivative of σ_e with equation (17), we get

$$\chi = 1 - \left[T \frac{\partial}{\partial T} \left(\frac{\partial g}{\partial \sigma_e} \right) - \frac{\partial g}{\partial \sigma_e} \right] \left(\frac{\rho \, \theta_0}{\sigma_y} \right) \left[1 - \left(\frac{\sigma_e}{\sigma_{es}} \right)^2 \right] \tag{43}$$

To model the specific Gibbs free energy $g(\widetilde{\boldsymbol{S}}, T, \sigma_e)$, we follow the approach of Schreyer and Maudlin [40] in postulating the following form for the expression involving the derivatives of g (which can be interpreted as a measure of the stored energy of cold work):

$$T \frac{\partial}{\partial T} \left(\frac{\partial g}{\partial \sigma_e} \right) - \frac{\partial g}{\partial \sigma_e} = F_1(T) \, F_2(\sigma_e) \tag{44}$$

where

$$F_1(T) = \frac{A_\chi}{1 + \exp\left[-B_\chi \left(1 - 2 \, \widehat{T} \right) \right]} ; \qquad F_2(\sigma_e) = \frac{1}{\rho_0} \left(\beta_\chi + \frac{\sigma_e}{\sigma_{es}} \right)^{1/2} . \tag{45}$$

where $A_\chi > 1, B_\chi > 1$ are constants, $\widehat{T} = T/T_m$ where T_m is the melting temperature, and $0 < \beta_\chi < 1$ is a factor that determines the value of χ at zero plastic strain. We can now calculate the rise in temperature due to plastic dissipation and use that to determine the amount of thermal softening due to plastic deformation. Note that a closed form expression for g that can be evaluated analytically cannot be derived from equation (44) and further investigation into possible forms of g is needed.

4. PARAMETER ESTIMATION FOR 6061-T6 ALUMINUM

Before the parameters of the extended MTS model for 6061-T6 aluminum can be estimated, we need the parameters of the shear modulus model. We also need the parameters of the associated melting temperature model, the equation of state model, and the specific heat model. A detailed exploration of various models, their parameters, and comparisons with experimental data can be found in [37]. The parameters of the models described by equations (26), (27), (29), (30), and (31) are given in Appendix A. We also show in Appendix A comparisons with experimental data of the predicted shear modulus, melting temperature, and specific heat.

4.1. **Athermal component.** In the ASM Handbook on nonferrous alloys [41] we find that, for quasistatic tensile loading, at 644 K the yield strength of 6061-T6 aluminum is 12 MPa. The ratio μ/μ_0 for this temperature is 0.65. Hence, the maximum possible value of τ_a at 644 K is 18 MPa. Since this component is athermal, that value must be an upper bound on τ_a. It is possible that the upper bound on τ_a is even lower since the melting temperature of aluminum at ambient pressure is around 933 K. Therefore it is reasonable to assume that $\tau_a \approx 10$ MPa for 6061-T6 aluminum.

4.2. **Intrinsic component.** To compute the intrinsic component of the flow stress (τ_i), we have to determine the parameters σ_{0i} and g_{0i} for a particular choice of $\dot{\varepsilon}_{0i}$, p_i, and q_i (see equation 4). From equation (25) we see that in the low to moderate strain rate regime, the flow stress at zero plastic strain can be written as

$$\sigma_y = \tau_v + (\tau_a + \tau_i)\,\frac{\mu}{\mu_0}\,. \tag{46}$$

To determine τ_i, we need the viscous drag component τ_v and the experimentally determined initial yield stress σ_y. Recent studies [42, 43] show that for strain rates less than 10^4 s^{-1}, the viscous drag component τ_v for 6061-T6 aluminum is small compared to the thermally activated component τ_i. Since the experimental stress-strain data that we have access to are for strain rates ranging from 10^{-5} s^{-1} to 8.0×10^3 s^{-1}, we neglect τ_v during the process of computation of σ_i and g_{0i}.

Then, from equations (46) and (4) we have

$$\left(\frac{\sigma_y}{\mu} - \frac{\tau_a}{\mu_0}\right)^{p_i} = \left(\frac{\sigma_i}{\mu_0}\right)^{p_i} - \left(\frac{\sigma_i}{\mu_0}\right)^{p_i}\left(\frac{1}{g_{0i}}\right)^{2/q_i}\left(\frac{k_b\,T}{b^3\,\mu}\ln\frac{\dot{\varepsilon}_{0i}}{\dot{\varepsilon}}\right)^{2/q_i} \tag{47}$$

which is of the form $y = A - B\,x^2$. A Fisher plot of the experimental data and the model fit is shown in Figure 1. Details of the procedure used to obtain the experimental data and the sources of the data can be found in [37]. The best fit to the experimental data is obtained for $p_i = 0.75$, $q_i = 1.0$, and $\dot{\varepsilon}_{0i} = 5.0\times10^8$ s^{-1}. The Boltzmann constant was taken to be $k_b = 1.38\times10^{-23}$ J/K and the magnitude of the Burgers' vector was assumed to be $b = 2.86\times10^{-10}$ m [44].

The fit shown in the figure has a R^2 value of 0.6, a F-statistic of 60.7 and Student's t-values of 6.0 and 35.3 for the two coefficients. There are 81 data points. Using a t-value of 1.663 (corresponding to the 95% interval), we get the following range of values for σ_i and g_{0i}: σ_i (low) = 343.7 MPa; σ_i (fit) = 366.6 MPa; σ_i (high) = 389.8 MPa; and g_{0i} (low) = 0.51; g_{0i} (fit) = 0.59; g_{0i} (high) = 0.71.

4.3. **Viscous drag component.** The viscous drag component of the flow stress is given by equation 5. Two quantities have to be determined before τ_v can be computed: the drag coefficient B and the mobile dislocation density ρ_m.

The drag coefficient can be estimated using either equation (6) or equation (10). Figure 2 shows the phonon drag coefficients predicted by the two models. The constants used for the models are $k_b = 1.38\times10^{-23}$ J/K, $b = 2.86\times10^{-10}$ m, $M = 26.98$ amu, $\rho_0 = 2700$ kg/m^3, $h = 6.62\times10^{-34}$ kg m^2/s, and $q = 3b$. Values of the Debye function (D_3) were calculated using an algorithm given in [19]. As the pressure increases there is a decrease in B_p. However the change is small and does not significantly affect the value of τ_v. At temperatures below 50 K, electron drag effects become dominant. Note that is this not reflected by the model in equation (10). However, since that model predicts a lower value of B_p at high temperatures, we have used (equation 10) in subsequent calculations.

The evolution of dislocation density is harder to quantify. We have chosen parameters for equations (13) in such a way that, at high strain rates, the viscous drag component of the flow stress approximates experimentally determined yield stress at room temperature. The parameters used for the model are: $b = 2.86$ m^{-2}, $M_1 = 4.14\times10^{-7}$, $I_{20} = 5.53\times10^3$, $I_3 = 3.81\times10^{-2}$, $\alpha_I = 1.0$, $\beta_I = 8.0$, $\rho_{fs0} = 1.0\times10^{14}$ m^{-2}, $\alpha_f = 0.4$, $\beta_f = 4.0$. Using initial values of $\rho_m = 1.0\times10^9$ m^{-2} and $\rho_f = 1.0\times10^{10}$ m^{-2}, we get the evolution of the dislocation densities shown in Figure 3. A constant density of 2700 kg-m^{-3} has been used in the computation.

The saturation value of ρ_m is approximately 2×10^{11} m^{-2} at room temperature, which is three orders of magnitude lower than that suggested by Estrin and Kubin [21]. However, higher values of ρ_m lead to unreasonably low values of the viscous drag component of the flow stress. Also, similar low values of ρ_m are suggested by Kumar and Kumble [10]. Note that the value of ρ_f is close to the accepted value of total

dislocation density in aluminum and its alloys of the order of 1.0×10^{14} m^{-2}. It can also be observed that the density of forest dislocations decreases with temperature while that of mobile dislocations increases with temperature. Also, our model indicates that the rate of annihilation of forest dislocations is greater than the rate of generation of mobile dislocations as the temperature increases (see Figure 3).

The viscous drag component (τ_v) of the flow stress can now be computed using equation 5. Figure 4 shows the variation of τ_v with strain rate and temperature (for a plastic strain of 0.2). We have used a value of $\lambda_p = 1$ in the calculations. From the figure it is clear that the viscous drag becomes significant only beyond strain rates of 10^5 s^{-1}. Also drag effects appear to be negligible at low temperatures.

4.4. **Structure evolution component.** To determine the structure evolution component (τ_e) of the flow stress we need to compute the evolution of the internal variable σ_e using equation (19). This equation requires two variables: the saturation value σ_{es} of σ_e and the initial hardening rate θ_0.

To compute σ_{es} using equation (21), we need the parameters σ_{0es}, g_{0es}, and $\dot{\varepsilon}_{0es}$. Given a set of true stress-true plastic strain curves, the first step in the process of determination of these parameters is to compute the temperature at each point on the curve (for experimental that data are not given in isothermal form). The temperature is computed using equation (40) with the value of χ being obtained using:

$$\chi = \min\{[0.019 - 0.089 \ln(\varepsilon_p) + 9.23 \, \varepsilon_p^2], 0.9\} \tag{48}$$

where ε_p is the true plastic strain. Equation (48) is a least squares fit to the experimental data for 2024-T351 aluminum given in [56]. The experimental σ_e versus true plastic strain curves are then computed using the relation

$$\sigma_e = \frac{1}{S_e}\left(\sigma_y \frac{\mu_0}{\mu} - \tau_a - \tau_i\right) . \tag{49}$$

Note that the quantity τ_i for each curve is the value used to compute the Fisher plot in Figure 1 unlike the procedure used elsewhere [2, 8]. The parameters used to compute S_e (see equation 16) are $k_b = 1.38 \times 10^{-23}$ J K^{-1}, $b = 2.86 \times 10^{-10}$ m^{-2}, $\dot{\varepsilon}_{0e} = 10^9$ s^{-1}, $g_{0e} = 3.0$, $p_e = 0.75$, and $q_e = 1.0$. The density is assumed to have a constant value of 2700 kg m^{-3} during deformation. Plots of σ_e versus ε_p for all the stress-strain curves used in this work can be found in [37].

After the σ_e versus ε_p curves have been computed, a quadratic polynomial is fit to each curve. The saturation value of σ_e and the temperature at saturation are computed by determining the strain at which the slope of the quadratic curve becomes zero. A Fisher plot can now be drawn to determine the values of σ_{0es} and g_{0es} by writing equation (21) in the form

$$\ln(\sigma_{es}) = \ln(\sigma_{0es}) - \frac{k_b \, T}{g_{0es} \, b^3 \, \mu} \ln\left(\frac{\dot{\varepsilon}_{0es}}{\dot{\varepsilon}}\right) . \tag{50}$$

To compute the Fisher plot we assume that $\dot{\varepsilon}_{0es} = 10^8$ s^{-1} and get the fit shown in Figure 5. The statistics of the fit are: $R^2 = 0.41$, F-statistic = 36.2, t-statistics = 6.0 and 157. There are 52 sample points. Therefore, though the fit is poor, it is statistically significant. The range of values of σ_{0es} and g_{0es} from the fit that are within the 95% confidence interval (corresponding to a t value of 1.675) are: σ_{0es} (low) = 122.3 MPa, σ_{0es} (fit) = 149.5 MPa, σ_{0es} (high) = 182.7 MPa, g_{0es} (low) = 0.235, g_{0es} (fit) = 0.30, g_{0es} (high) = 0.416.

To compute the initial hardening rate (θ_0), we first compute the slopes (θ) of the σ_e versus ε_p curves at each point on the curve. The slope θ is then plotted against $1 - (\sigma_e/\sigma_e s)^2$ and a straight line with zero intercept is fitted to the resulting curve. This model gives a better fit to the experimental data that the more commonly used hyperbolic tangent hardening rule [1, 2, 8]. The slope of the straight line fit gives us the value of θ_0 for each curve. A least squares surface fit of θ_0 as a function of strain rate and temperature (assuming that the parameter $\dot{\varepsilon}_\theta = 10^{10}$ s^{-1}) gives us the following parameters for equation

(20): a_0 = 0.147, a_1 = -2.4×10^{-3}, a_2 = -0.14, a_3 = 3.3×10^{-3}. The spread of the data is quite large and the R^2 value for the fit is 0.38. The F-statistic for the fit is 3.2 which implies that the fit may not be statistically significant. However, comparisons with experimental data show that the predicted flow stresses are reasonable when we use the above parameters. For the details of an alternative approach for modeling the hardening of 6061-T6 aluminum in the context of the MTS model see [37].

4.5. **Overdriven shock regime.** In the overdriven shock regime, we assume that the flow stress is given by equation (22) and that the material does not harden. The parameters of the model are determined by fitting a curve to experimental data on 1100 Al and 2024 Al from [57]. We assume that 6061-T6 Al also shows a similar behavior. The fit to the data is shown in Figure 6. The following parameters have been used in the calculation: ρ_0 = 2700 kg m^{-3}, ρ = 2710 kg m^{-3}, T = 298 K, σ_{ys0} = 700 MPa, M = 26.98 amu, and γ = 0.0001. The parameters determined from the fit are: y_1 = 3.54×10^{-3} and y_2 = 0.5.

4.6. **Taylor-Quinney Coefficient.** The Taylor-Quinney coefficient (χ) can be computed using equation (43). To evaluate this equation we need the parameters A_χ, B_χ, and β_χ in equations (45). We have determined these parameters by comparing the predictions of our model with experimental data for 2024-T3 aluminum from [39]. Figures 7(a) and (b) show the predicted values of χ for initial temperatures of 300 K and 500 K, respectively. The parameters used for the plots are A_χ = 0.2, B_χ = 12, and β_χ = 0.3. A constant mass density of 2700 kg m^{-3} was used for the calculations. Note that these parameters will change if θ_0 or σ_{es} are changed.

From Figure 7(a) we observe that, at a temperature of 300 K, the values of χ are nearly the same for strain rates between 0.001 s^{-1} to 3000 s^{-1}. This is similar to the experimental observations in [39]. However, the value of χ increases as the flow stress increases with increasing strain rate due to viscous drag effects. This effect is similar to that observed in rate-dependent α-titanium in [39]. Hence, our model behaves is a reasonable manner at room temperature. On the other hand, the experimental data for 2024-T3 aluminum indicates that low values of χ (less than 0.5) are obtained up to a plastic strain of around 0.3 while our model predicts such values only up to a plastic strain of 0.05. The width of this zone depends on the initial hardening modulus (θ_0) and on the saturation stress (σ_{es}). The discrepancy between our model for 6061-T6 aluminum and the experimental data for 2024-T3 aluminum indicates that θ_0 for 2024-T3 aluminum might be lower than that for 6064-T6 aluminum. It is also possible that the saturation stress computed by our model is lower than should be expected.

At 500 K (see Figure 7(b)), the value of χ is considerably higher than at 300 K. We do not have any experimental data to verify that this behavior is reasonable. Experiments at high temperatures are needed to arrive at the correct form of the function $F_1(T)$ in equation (44). As designed, our the model predicts values of χ close to 1.0 at high temperatures. However, experiments are needed to verify that this is indeed the case for metals and that the stored energy approaches zero at high temperatures.

5. Comparisons of model with experimental data

The verification of the extended MTS flow stress model presented in this paper can be pursued in a number of ways. The strain rate dependence of the model can be verified by computing the flow stress as a function of strain rate (at a constant temperature and plastic strain) and comparing the predicted values with experimental data. A similar comparison of the flow stress as a function of temperature (with the strain rate kept constant) can be used to verify the temperature dependence of the model. Direct comparisons with uniaxial stress-strain curves can also be performed for various strain rates and temperatures.

Numerical simulation is necessary for a more comprehensive validation of the model. Examples of such numerical validation tests have been provided in [37]. Details of the numerical algorithm and various validation tests will be discussed in a forthcoming publication.

5.1. **Flow stress as a function of strain rate.** Figure 8 shows a comparison of the flow stress predicted by the extended MTS model with experimental data (as a function of strain rate). In the computations performed, the evolution equations for dislocation density were not solved because of the excessive computational cost involved. Rather, a constant value of $\rho_m = 2.0 \times 10^{11}$ m^{-2} and a scaling factor of λ_p = 1.0 were used to compute the component of the flow stress due to viscous drag (τ_v). Adiabatic heating is assumed for strain rates greater than 100 s^{-1}.

Experimental data from [49, 55, 43] for 6061-T6 aluminum alloy suggest that viscous drag effects are small for strain rates up to 3×10^4 s^{-1}. This is in contrast with data given in [54] which suggests that drag effects become important at strain rates of 10^4 s^{-1} or less. Sakino [43] has shown quite convincingly that drag effects become important at lower strain rates only in the annealed alloy 6061-O aluminum but not in the hardened 6061-T6 aluminum alloy. Our model slightly overestimates the flow stress for strain rates less than 10^5 s^{-1} but matches quite well with the available data for higher strain rates. The 95% confidence interval shown in the figure is based on the low and high values of σ_i, g_{0i}, σ_{0es}, and g_{0es} discussed earlier.

From Figure 8 we can also observe a change in slope of the flow stress-strain rate curve at a strain rate of around 10^6 s^{-1}. Experimental data are not available for the strain rate regime between 10^6 s^{-1} and 10^{10} s^{-1}. The curves for the overdriven shock regime and the moderate strain rate regime can be matched only if there is a change in slope as shown in the figure. A better model for the intermediate strain rate regime can only be determined after experiments (or possibly numerical simulations) have been performed for this regime. In the model that we have presented in this paper, we assume that the viscous drag component of the flow stress saturates when σ_y reaches a value of 700 MPa and any additional increase in the flow stress is due to shock effects as discussed in [58, 59].

5.2. **Flow stress as a function of temperature.** Figures 9(a) and (b) show comparisons between experimental data and the flow stress predicted by our model as a function of temperature. At low strain rates (see Figure 9(a)), the decrease in flow stress with temperature is predicted quite accurately by the model. Near the melting temperature, the contributions of τ_i and τ_e are close to zero and the flow stress is determined by the athermal component τ_a. Beyond the melting temperature, the stress is computed by the Newtonian fluid model in equation 24 and the stress is quite small at low strain rates. Adiabatic heat is assumed for the high strain rate calculations.

At a strain rate of 1000 s^{-1}, our model predicts the flow stress quite well up to $T/T_m = 0.6$ (see Figure 9(b)). At higher temperatures, the flow stress is overestimated. The prediction of our model is reasonable if we consider the full set of data used to arrive at the parameters. It is expected that the predicted temperature dependence of our model can be improved at more experimental data at high temperatures and high strain rates become available.

5.3. **Flow stress as a function of pressure.** Figure 10 shows the predicted pressure dependence of the flow stress of 6061-T6 aluminum at a strain rate of 0.001 s^{-1}. The increase in flow stress with increasing pressure is underestimated by our model. Since the pressure dependence of the flow stress at low strain rates is determined by the pressure dependence of the shear modulus, the figure shows that the pressure dependence of the shear modulus is not enough to account for the pressure dependence of the flow stress. We also observe that

$$\frac{\partial \sigma_y}{\partial p} \approx 2 \, \frac{\partial \mu}{\partial p} \, . \tag{51}$$

This suggests that the pressure dependence of the flow stress in the Steinberg-Cochran-Guinan model [34] (which is used widely for high strain rate calculations and assumes that $\partial \sigma_y / \partial p \approx \partial \mu / \partial p$) is not correct. We have also observed a similar behavior for OFHC copper [61]. An explicit pressure dependence of the initial hardening modulus and the saturation stress is needed to model the plastic behavior of metals

under hydrostatic pressure. Such a dependence has to be based on physical considerations and needs further research.

5.4. Uniaxial stress-strain curves.
The predicted variation of the flow stress with plastic strain at a strain rate of 0.001 s^{-1} is shown in Figure 11. The calculations were performed using a constant mass density of 2700 kg m^3, and a constant mobile dislocation density of 2×10^{11} m^{-2}. Isothermal conditions were assumed.

Figure 11(a) shows the predicted flow stress at ambient pressure. The flow stress predicted by our model tends to saturate at a lower value than seen in the experimental data. Also the predicted initial hardening modulus is lower than that suggested by the experiments at 367 K and 422 K and higher than experiment at 589 K. However, the initial yield stress predicted by our model is remarkably close to that seen in experiments considering the experimental variability that is observed (for further data on experimental variability at a given temperature and strain rate see [37]). The experimental stress-strain curves show strain softening. A damage model that includes void nucleation and growth can be used to predict that portion of the stress-strain curve. For the sake of simplicity, we do not discuss damage models and their implications in this paper.

Figure 11(b) shows the predicted flow stress at a pressure of 276 MPa. We notice that the initial yield stress is predicted quite accurately by our model at this pressure for all the temperatures shown in the figure. However, the hardening rate and the saturation stress are underestimated. The error decreases with increasing temperature. Similar plots at higher pressures show that the error increases with increasing pressure at a particular temperature (see also Figure 10). As mentioned before, an explicit pressure dependence of the initial hardening rate and the saturation stress is needed to improve our model.

Figures 12(a) and (b) show the predicted stress-strain curves for strain rates greater than 1000 s^{-1}. The change in mass density due to large pressures that develop at such strain rates has been neglected in our computations. To keep the computations efficient, we have not used the evolution equations for dislocation density and have instead used a constant value of $\rho_m = 2 \times 10^{11}$ m^{-2}. Adiabatic heating and the resulting thermal softening has been assumed for all these computations.

From Figure 12(a) we observe that the flow stress predicted by the extended MTS model matches well with the experimental data for temperatures of 77K and 298K. At 473 K, the predicted flow stress is higher than experiment and does not capture the strain softening due to accumulating damage in the material. At 618K, the predicted flow stress is considerably higher than experiments suggest. As observed before, our model does not predict enough thermal softening of 6061-T6 aluminum at higher temperatures - particularly at high strain rates. It is important to note here that 6061-T6 aluminum is a precipitation hardened alloy containing magnesium and silicon as alloying elements. At about 550K, the solute molecules start to diffuse toward the grain boundaries and the alloy softens considerably. Though the extended MTS model is an improvement over the original MTS model (see [37] for similar results with the original MTS model), the amount of thermal softening continues to be overestimated by the extended model.

Figure 12(b) shows that the experimental data does not show any significant strain rate dependence at room temperature (at least up to a strain rate of 29,000 s^{-1}). Our model predicts a small increase in flow stress with strain rate and some thermal softening at strains greater than 0.2. However, the overall match with experiment is quite good. Also the initial rate of hardening appears to be lower than that predicted. However, stress-strain data from split Hopkinson pressure bar experiments are suspect for strains less than 0.1 and conclusions cannot be drawn about the accuracy of our hardening model from this figure.

6. MODEL PREDICTIONS

In this section we discuss the predictions of our flow stress model for a large range of conditions. The mass density is assumed to be constant (2700 kg m^{-3}) in our calculations. Since the phonon drag coefficient increases with temperature, assuming a constant mobile dislocation density for all temperatures gives unrealistic flow stresses at strain rates greater than 10^4 s^{-1}. On the other hand, using the evolution equations to determine ρ_m is not computationally efficient. Hence we have used the following equation to determine ρ_m for our calculations in this section:

$$\rho_m \approx \rho_{m0}(1 + \widehat{T})^m \tag{52}$$

where ρ_{m0} is the dislocation density at 0 K, $\widehat{T} = T/T_m$ where T_m is the melting temperature, and m is a constant. The values of these parameters that we have use are: $\rho_{m0} = 1.3494 \times 10^{11}$ m^{-2} and $m = 1.4114$. Using these parameters gives us a value of $\rho_m = 2 \times 10^{11}$ m^{-2} at 300 K and $\rho_m = 3.5 \times 10^{11}$ m^{-2} at 900 K. The value of ρ_m is not allowed to vary with plastic strain.

Figure 13(a) shows the flow stress predicted by our model as a function of strain rate at a plastic strain of 0.2 and for a range of temperatures. From the figure we observe that at low strain rates, the flow stress is strongly dependent on temperature. As the strain rate reaches around 10^5 s^{-1}, the model predicts that the temperature dependence of the flow stress decreases until the temperature has hardly any effect.

Figure 13(b) shows the flow stress as a function of strain rate at a temperature of 400 K and for various levels of strain. In this case we observe that the flow stress saturates rather rapidly (at a plastic strain of around 0.2). This indicates that the material exhibits little strain hardening. However, simulations of Taylor impact tests (see [37]) indicate that we underestimate the amount of hardening in our model. A value of the initial hardening modulus (θ_0) that is around 0.3 of the value that we have used gives a more realistic amount of hardening. However, such a value leads to an underestimation of the flow stress at low strain rates. A better hardening model than the one used is clearly needed if we are to predict the saturation strain more accurately.

Figure 14(a) shows the flow stress predicted by our model as a function of temperature at a plastic strain of 0.2 and for a range of strain rates. At low strain rates the flow stress decreases rapidly with temperature until it reaches the athermal value. For a strain rate of 10^3 s^{-1} and higher the initial decrease of the flow stress with temperature is small. However, as the temperature reaches the melting temperature, the flow stress drops abruptly to a small value (determined by the constitutive relation for a Newtonian fluid). In the absence of experimental data, it is not obvious whether this behavior of our model accurately represents reality.

Figure 14(b) shows the flow stress as a function of temperature at a strain rate of 8000 s^{-1} and for various levels of strain. Once again, we see that the flow stress saturates at a plastic strain of about 0.2. At low temperatures, the material hardens significantly before saturation. However, as the temperature increases the amount of hardening decreases until at around 850 K there is essentially no hardening. This is reasonable behavior considering the fact that thermally activated dislocation motion is dominant in at a strain rate of 8000 s^{-1} and enough thermal energy is available at high temperatures to allow slip to occur more readily. The convex nature of the curves shown in the figure also indicate that we are able to capture some of the effects of high temperature solute diffusion in our model.

In Figure 15(a) we have plotted the predicted flow stress as a function of plastic strain. The strain rate is 8000 s^{-1} and the initial temperatures range from 50 K to 900 K. Adiabatic heating is assumed and the temperature increases with increasing strain. All the curves show a small amount of thermal softening. We also observe that the initial rate of hardening decreases with temperature. Saturation is reached at higher strains as the temperature increases. If we compare the flow stress at 300 K with those shown in Figure 12(b), we observe that there is hardly any strain rate dependence at these strain rates. We also

observe that the flow stress at 900 K is around 70 MPa which is high considering the fact that the material is close to its melting point.

Figure 15(b) shows stress-strain plots at various strain rates. The initial temperature of the material is 400 K in these plots. Isothermal conditions were assumed for strain rates lower than 1000 s^{-1} and adiabatic conditions otherwise. Interestingly, the only curve that shows an appreciable amount of thermal softening is the curve at 1000 s^{-1}. At a strain rate of 10^5 s^{-1}, the increase in the drag coefficient with temperature offsets the amount of thermal softening that occurs. The temperature dependence of the flow stress at a strain rate of 10^7 s^{-1} is negligible and hence there is no appreciable thermal softening with increasing strain. The amount of strain that can be achieved at high strain rates is not clear and failure will probably occur before a plastic strain of 0.6 is achieved.

7. Concluding Remarks

One of the main shortcomings of the original mechanical threshold stress model was that it was not accurate at strain rates greater than about 10^4 s^{-1}. In this paper we have presented an extended mechanical threshold stress model that is valid for strain rates at which viscous drag effects become dominant. The model has also been extended to the overdriven shock regime. The original model of Follansbee and Kocks was also designed for use in the temperature regime where solute diffusion and other thermally activated diffusion effects could be neglected (typically less than 0.6 of the melting temperature). In the extended model, we allow for higher temperatures by using a modified form of the equation for the intrinsic component of the flow stress. The strain rate dependence of the flow stress is predicted quite accurately by our model. However, the predicted temperature dependence is less accurate and could be improved. Since the density of obstacles inside a crystal decreases with increasing temperature, the activation energy should be a function of the temperature. It is possible that a temperature-dependent model for the activation energy will improve predictions of the flow stress of 6061-T6 aluminum at high temperatures. More high temperature-high strain rate data of the type provided by Rosenberg et al. [23] are essential before such a model can be developed.

We have provided a detailed description of the procedure for calculating the drag stress. Two methods for computing the viscous drag coefficient have been compared in the paper. We have found that Liebfried's theory provides an estimate of the viscous drag coefficient that better matches experiment. We have also added a temperature dependence to the dislocation evolution equations of Estrin and Kubin and determined new parameters for these equations that fit experimental data. Estrin and Kubin have estimated that the mobile dislocation density is around 10^{14} m^{-2} at saturation. Our results suggest that a more accurate estimate of this quantity is 2×10^{11} m^{-2}.

The evolution equations of the internal variable (mechanical threshold stress) have been simplified and a non-dimensional form for the initial hardening modulus has been proposed. The simplified equations allow for an exact expression for the internal variable as a function of plastic strain which can be evaluated efficiently in a computational code. Alternatively, we could have used the equations for the evolution of the dislocation density with the dislocation density as an internal variable. However, the system of equations involved is very stiff and computationally expensive to solve for high strain rate problems. The parameters for 6061-T6 aluminum alloy (needed for the evolution of the internal variable) that we have determined in this paper lead to an underestimation of the saturation stress and the amount of hardening. This effect is particularly noticeable for high hydrostatic pressures. Also, the pressure dependence of the flow stress is not reflected completely by the pressure dependence of the shear modulus (for which a model is presented in the paper). Explicitly pressure dependent models for the hardening modulus and the saturation stress are clearly needed.

In addition, we have developed an equation for the evolution of temperature with plastic strain based on thermodynamic principles. An expression has been presented for the Taylor-Quinney coefficient as

a function of the mechanical threshold stress internal variable. This expression requires a functional representation of the Gibbs free energy density. We have postulated a form of the derivatives of this function that matches experimental data qualitatively. However, further research is needed to arrive at a better form of the Gibbs free energy density function.

Important issues that have not been addressed in this paper are cyclic loading and kinematic hardening models, deformation induced anisotropy in both the elastic and plastic behavior, the appropriate form of the yield condition and the flow rule, and the modeling of void nucleation and growth and the accompanying elastic and plastic damage. Also, in this paper, we have considered only one dimensional analytical verification tests. Consideration of some of the above issues and detailed numerical validation experiments using the Material Point Method [62, 63] are in progress and will be the subject of a subsequent paper.

8. ACKNOWLEDGEMENTS

APPENDIX A. SPECIFIC HEAT, EOS, MELTING TEMPERATURE, SHEAR MODULUS

Experimental data indicate that the specific heat (at constant pressure) of aluminum increases by around 37% between room temperature and melting [64]. A least squares curve fit to the experimental data yields the following parameters for the model given in equation (31): A_1 = -11.73 J/kg-K, B_1 = 6.28 J/kg-K^2, C_1 = -0.011 J/kg-K^3, A_2 = 743.13 J/kg-K, and B_2 = 0.51 J/kg-K^2. A plot of the fit is shown in Figure 16.

The shear modulus model given in equation (26) requires a pressure. We use the equation of state (EOS) in equation (30) to compute the pressure for a given change in density. The parameters that we have used for 6061-T6 aluminum are B_0 = 76.3 GPa and B_0' = 4.29 [31]. Experimental data for 6061-T6 aluminum alloy [65], 2024-O aluminum alloy [66], and pure aluminum [67] are closely matched by the EOS model up to a compression ratio (ρ/ρ_0) of 1.4.

Though the alloying content can have a significant effect of the melting temperature of metals, we have assumed in this paper that the melting temperature of 6061-T6 aluminum does not differ significantly from that of pure aluminum. The parameters of the model of melting temperature given in equation (29) for 6061-T6 aluminum are taken to be T_{m0} = 933.6 K, q = 3.3, Γ_1 = 0.84 (gm/cc)$^{1/3}$, and Γ_2 = 45.4 (gm/cc)^q. We also assume that for hydrostatic tensile states the melting temperature is equal to T_{m0}. The prediction of the model of equation (29) is compared with experimental data in Figure 17. An initial density of 2700 kg/m^3 was used while computing the quantities in the figure. The model fits the data from Boehler and Ross ([68]) quite well (triangles) but not the older data collected in [69] (circles). The accuracy of the Boehler and Ross data has been confirmed by more recent numerical experiments by Vocadlo and Alfe ([70]).

The shear modulus model in equation (26) allows for a smooth transition to zero shear modulus beyond melting. This feature is advantageous in numerical simulations for conditions where melting might occur. The parameters of the shear modulus model for 6061-T6 aluminum are μ_0 = 31.3 GPa, $\partial\mu/\partial p$ = 1.8 [71], a_1 = 0.53, a_2 = 0.10, a_3 = 0.37 [31], C = 0.049 [30], ζ = 0.1, and m = 26.98 amu. The predicted shear modulus as a function of temperature is compared with experimental data in Figure 18(a). An initial density of 2700 kg/m^3 was used for the calculations in the figure. Further details and comparisons with other models can be found in [37].

The density dependence of the shear modulus at 0 K is compared with computed results in Figure 18(b). Since the pressure depends directly on the density in the equation of state, this plot may also be considered to be a measure of the pressure dependence of the shear modulus. Our model predicts the shear modulus quite accurately up to $\rho/\rho_0 = 2.2$. Beyond this point the material undergoes a phase transition to the bcc phase and our model overestimates the shear modulus with increasing pressure.

REFERENCES

[1] P. S. Follansbee and U. F. Kocks. A constitutive description of the deformation of copper based on the use of the mechanical threshold stress as an internal state variable. *Acta Metall.*, 36:82–93, 1988.

[2] D. M. Goto, J. F. Bingert, S. R. Chen, G. T. Gray, and R. K. Garrett. The mechanical threshold stress constitutive-strength model description of HY-100 steel. *Metallurgical and Materials Transactions A*, 31A:1985–1996, 2000.

[3] U. F. Kocks. Realistic constitutive relations for metal plasticity. *Materials Science and Engrg.*, A317:181–187, 2001.

[4] M. Epler. Structures by precipitation from solid solution. In *Metallography and Microstructures. ASM Handbook: Volume 9*, pages 134–139. ASM International, New York, 2002.

[5] E. S. Puchi-Cabrera, C. Villabos-Gutiérres, and G. Castro-Fariñas. On the mechanical threshold stress of aluminum: Effect of the alloying content. *ASME J. Engg. Mater. Tech.*, 123:155–161, April 2001.

[6] B. Banerjee. Validation of UINTAH: Taylor impact and plasticity models. In *Proc. 2005 Joint ASME/ASCE/SES Conference on Mechanics and Materials (McMat 2005)*, Baton Rouge, LA, 2005.

[7] F. J. Zerilli and R. W. Armstrong. Dislocation-mechanics-based constitutive relations for material dynamics calculations. *J. Appl. Phys.*, 61(5):1816–1825, 1987.

[8] B. Banerjee. The Mechanical Threshold Stress model for various tempers of 4340 steel. *Int. J. Solids Struct.*, 44(3-4):834–859, 2007.

[9] U. F. Kocks, A. S. Argon, and M. F. Ashby. Thermodynamics and kinetics of slip. In B. Chalmers, J. W. Christian, and T. B. Massalski, editors, *Progress in Materials Science: Volume 19*, pages 1–289. Pergamon Press, Oxford, 1975.

[10] A. Kumar and R. G. Kumble. Viscous drag on dislocations at high strain rates in copper. *J. Appl. Phys.*, 40(9):3475–3480, 1969.

[11] H. J. Frost and M. F. Ashby. Motion of a dislocation acted on by a viscous drag through an array of discrete obstacles. *J. Appl. Phys.*, 42(13):5273–5279, 1971.

[12] W. G. Wolfer. Phonon drag on dislocations at high pressures. Technical Report UCRL-ID-136221, Lawrence Livermore National Laboratory, Livermore, California, 1999.

[13] E. Nadgornyi. Dislocation dynamics and mechanical properties of crystals. In J. W. Christian, P. Haasen, and T. B. Massalski, editors, *Progress in Materials Science: Volume 31*, pages 1–530. Pergamon Press, Oxford, 1988.

[14] G. I. Kanel, S. V. Razorenov, K. Baumung, and J. Singer. Dynamic yield and tensile strength of aluminum single crystals at temperatures up to the melting point. *J. Appl. Phys.*, 90(1):136–143, 2001.

[15] A. D. Brailsford. Phonon component of dislocation drag. *J. Appl. Phys.*, 41(11):4439–4442, 1970.

[16] A. D. Brailsford. Anharmonicity contributions to dislocation drag. *J. Appl. Phys.*, 43(4):1380–1393, 1972.

[17] C. Truesdell. On a function which occurs in the theory of the structure of polymers. *The Annals of Mathematics: Series 2*, 46(1):144–157, 1945.

[18] E. W. Ng, C. J. Devine, and R. F. Tooper. Chebyshev polynomial expansion of bose-einstein functions of order 1 to 10. *Mathematics of Computation*, 23(107):639–643, 1969.

[19] A. MacLeod. Algorithm 757, MISCFUN: A software package to compute uncommon special functions. *ACM Transactions on Mathematical Software*, 22(3):288–301, 1996.

[20] I. A. Stegun. Miscellaneous functions. In *Handbook of Mathematical Functions with Formulas, Graphs, and Mathematical Tables*, pages 997–1010. Dover, New York, 1972.

[21] Y. Estrin and L. P. Kubin. Local strain hardening and nonuniformity of plastic deformation. *Acta Metall.*, 34(12):2455–2464, 1986.

[22] F. Barlat, M. V. Glazov, J. C. Brem, and D. J. Lege. A simple model for dislocation behavior, strain and strain rate hardening evolution in deforming aluminum alloys. *Int. J. Plasticity*, 18:919–939, 2002.

[23] Z. Rosenberg, D. Dawicke, E. Strader, and S.J. Bless. A new technique for heating specimens in split-Hopkinson-bar experiments using induction-coil heaters. *Exp. Mechanics*, 26(3):157–173, 1986.

[24] D. L. Preston, D. L. Tonks, and D. C. Wallace. Model of plastic deformation for extreme loading conditions. *J. Appl. Phys.*, 93(1):211–220, 2003.

[25] E. N. da Andrade. The theory of viscosity of liquids: I. *Philosphical Magazine*, 17:497, 1934.

[26] E. N. da Andrade. Viscosity of liquids. *Proc. R. Soc. Lond. A*, 215(1120):36–43, 1952.

[27] J. G. Kirkwood, F. P. Buff, and M. S. Green. The statistical mechanical theory of transport processes: III. T coefficients of shear and bulk viscosity of liquids. *The J. Chem. Phys.*, 17(19):988–994, 1949.

[28] A. T. Dinsdale and P. N. Quested. The viscosity of aluminum and its alloys - A review of data and models. *J. Materials Science*, 39:7221–7228, 2004.

[29] E. A. Moelwyn-Hughes. *Physical Chemistry: 2nd Edition*. Pergamon, Oxford, 1961.

[30] M.-H. Nadal and P. Le Poac. Continuous model for the shear modulus as a function of pressure and temperature up to the melting point: analysis and ultrasonic validation. *J. Appl. Phys.*, 93(5):2472–2480, 2003.

[31] L. Burakovsky and D. L. Preston. Generalized Guinan-Steinberg formula for the shear modulus at all pressures. *Phys. Rev. B*, 71:184118–1–7, 2005.

[32] M. W. Guinan and D. J. Steinberg. A simple approach to extrapolating measured polycrystalline shear moduli to very high pressure. *J. Phys. Chem. Solids*, 36:829–829, 1975.

[33] L. Burakovsky, C. W. Greeff, and D. L. Preston. Analytic model of the shear modulus at all temperatures and densities. *Phys. Rev. B*, 67:094107–1–9, 2003.

[34] D. J. Steinberg, S. G. Cochran, and M. W. Guinan. A constitutive model for metals applicable at high-strain rate. *J. Appl. Phys.*, 51(3):1498–1504, 1980.

[35] W. B. Holzapfel. Equation of state for ideal and real solids under strong compression. *Europhysics Letters*, 16:67–72, 1991.

[36] W. B. Holzapfel. Equation of state for solids under strong compression. *High Pressure Research*, 7:290–293, 1991.

[37] A. Bhawalkar. The mechanical threshold stress plasticity model for 6061-T6 aluminum alloy and its numerical validation. Master's thesis, Department of Mechanical Engineering, University of Utah, Salt Lake City, UT, USA, 2006.

[38] T. W. Wright. *The Physics and Mathematics of Adiabatic Shear Bands*. Cambridge University Press, Cambridge, UK, 2002.

[39] J. Hodowany, G. Ravichandran, A. J. Rosakis, and P. Rosakis. Partition of plastic work into heat and stored energy in metals. *Experimental Mechanics*, 40(2):113–123, 2000.

[40] H. L. Schreyer and P. J. Maudlin. Thermodynamically consistent relations involving plasticity, internal energy and thermal effects. *Phil. Trans. R. Soc. A*, 363:2517–2541, 2005.

[41] ASM International Handbook Committee. *American Society of Metals Handbook: Volume 2*. American Society of Metals, New York, 2002.

[42] K. Ogawa. Impact tensile characteristics of 6061-T6 aluminum alloy. *Journal of Japan Institute of Light Metals*, 51(3):175–181, 2001.

[43] K. Sakino. Strain rate dependence of dynamic flow stress considering viscous drag for 6061 aluminum alloy at high strain rates. *J. Phys. IV France*, 134:183–189, 2006.

[44] J. Wang, Q. F. Fang, and Z. G. Zhu. Sensitivity of ultrasonic attenuation and velocity change to cyclic deformation in pure aluminum. *Phys. Stat. Sol.*, 169:43–48, 1998.

[45] K. G. Hoge. Influence of strain rate on mechanical properties of 6061-T6 aluminum under uniaxial and biaxial states of stress. *Experimental Mechanics*, 6:204–211, 1966.

[46] S. J. Green and S. G. Babcock. High strain rate properties of eleven reentry-vehicle materials at elevated temperatures. Technical Report AFFDL-TR-67-35, DASA, 1966. Part I of Final Report for DASA contract DA-49-149-XZ-322.

[47] A. M. Eleiche. Experimental investigations in the stress-strain charactesistics of polycrystalline metals and alloys at high strain-rates and elevated temperatures - survey. Master's thesis, Division of Engineering, Brown University, 1972.

[48] P. G. Davidson. *The effects of high pressure and temperature environments on the properties of 6061-T651 Aluminum*. PhD thesis, Department of mechanical engineering, University of Missouri-Rolls, Rolla, MO, 1973.

[49] S. Yadav, D. Chichili, and K. Ramesh. The mechanical response of 6061-T6 Al/Al$_2$O$_3$ metal matrix composite at high rates of deformation. *Acta Metall. Mater.*, 43:4453–4464, 1995.

[50] W.F. Brown, H. Mindlin, and C. Y. Ho. *Aerospace structural metals handbook: Volume 3: Code 3206*. CINDAS/USAF CRDA Handbooks Operation, Purdue University, West Lafayette, IN., 1996.

[51] W. S. Lee, J.C. Shyu, and S. T. Chiou. Effect of strain rate on impact response and dislocation substructure of 6061-T6 aluminum alloy. *Scripta Materialia*, 42:51–56, 2000.

[52] C. M. Cady and G. T. Gray III. Influence of strain rate on the deformation and fracture response of a 6061-T6 Al-50 vol. % Al$_2$O$_3$ continuous-reinforced composite. *Material Science and Engineering*, A298:56–62, 2001.

[53] J. Fish, C. Oskay, R. Fan, and R. Barsoum. Al 6061-T6-elastomer impact simulations. Electronic document, 2005.

[54] D. R. Lesuer, G. J. Kay, and M. M. LeBlanc. Modeling large-strain, high-rate deformation in metals. Technical Report UCRL-JC-134118, Lawrence Livermore National Laboratory, Livermore, CA, 2001. Johnson-Cook plasticity model for 6061T6 Aluminum.

[55] D. Jia and K. T. Ramesh. A rigorous assessment of the benefits of miniaturization in the Kolsky bar system. *Expt. Mechanics*, 44(5):445–454, 2004.

[56] G. Ravichandran, A. J. Rosakis, J. Hodowany, and P. Rosakis. On the conversion of plastic work into heat during high-strain-rate deformation. In *Proc. , 12th APS Topical Conference on Shock Compression of Condensed Matter*, pages 557–562. American Physical Society, 2001.

[57] D. L. Tonks. Deviatoric stresses and plastic strain rates in strong shock waves for six metals. Report LA-12641, Los Alamos National Laboratory, New Mexico, 1993.

[58] D. C. Wallace. Irreversible thermodynamics of overdriven shocks in solids. *Physical Review B*, 24(10):5597–5606, 1981.

[59] D. C. Wallace. Nature of the process of overdriven shocks in metals. *Physical Review B*, 24(10):5607–5615, 1981.

[60] J. J. Dike, J. A. Brooks, D. J. Bammann, and M. Li. Thermal-mechanical modeling and experimental validation of weld solidification cracking in 6061-T6 aluminum. Technical Report SAND-97-8582C, Sandia National Laboratories, Albuquerque, New Mexico, 1997.

[61] B. Banerjee. An evaluation of plastic flow stress models for the simulation of high-temperature and high strain-rate deformation of metals. *arXiv:cond-mat*, 0512466:1–43, 2005.

[62] D. Sulsky, Z. Chen, and H. L. Schreyer. A particle method for history dependent materials. *Comput. Methods Appl. Mech. Engrg.*, 118:179–196, 1994.

[63] D. Sulsky, S. Zhou, and H. L. Schreyer. Application of a particle-in-cell method to solid mechanics. *Computer Physics Communications*, 87:236–252, 1995.

[64] P. D. Desai. Thermodynamic properties of aluminum. *Int. J. Thermophysics*, 8(5):621–638, 1987.

[65] S. N. Vaidya and Kennedy G. C. Compressibility of 18 metals to 45 kbar. *Phys. Chem. Solids*, 31:2329–2345, 1970.

[66] R. G. McQueen, S. P. Marsh, J. W. Taylor, J. N. Fritz, and W. J. Carter. The equation of state of solids from shock wave studies. In R. Kinslow, editor, *High Velocity Impact Phenomena*, pages 294–417. Academic Press, New York, 1970.

[67] A. C. Mitchell and W. J. Nellis. Shock compression of aluminum, copper, and tantalum. *J. Appl. Phys.*, 52(5):3363–3374, 1981.

[68] R. Boehler and M. Ross. Melting curve of aluminum in a diamond cell to 0.8 Mbar: implications for iron. *Earth and Planetary Science Letters*, 153:223–227, 1997.

[69] L. Burakovsky, D. L. Preston, and R. R. Silbar. Melting as a dislocation-mediated phase transition. *Phys. Rev. B*, 61(22):15011–15018, 2000.

[70] L. Vocadlo and D. Alfe. Ab initio melting curve of the fcc phase of aluminum. *Physical Rev. B*, 65:214105–1–12, 2002.

[71] M. W. Guinan and D. J. Steinberg. Pressure and temperature derivatives of the isotropic polycrystalline shear modulus for 65 elements. *J. Phys. Chem. Solids*, 35:1501–1512, 1974.

[72] J. L. Tallon and A. Wolfenden. Temperature dependence of the elastic constants of aluminum. *J. Phys. Chem. Solids*, 40:831–837, 1979.

DEPARTMENT OF MECHANICAL ENGINEERING, UNIVERSITY OF UTAH, 50 S CENTRAL CAMPUS DR RM 2110, SALT LAKE CITY, UT 84112, USA

E-mail address: banerjee@eng.utah.edu

ENGINEER, BRAHMA GROUP, INC., 570 WEST 800 SOUTH, SALT LAKE CITY, UT 84101, USA
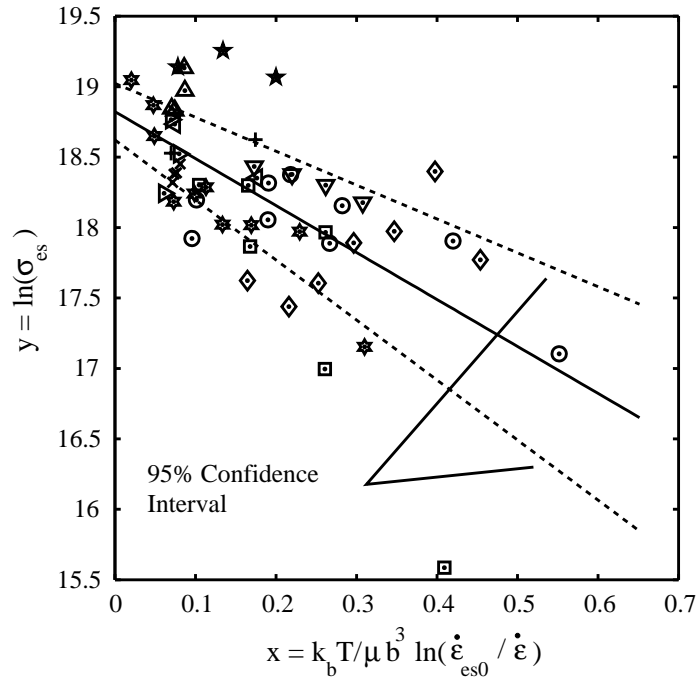
E-mail address: anupb@brahmagroupinc.com
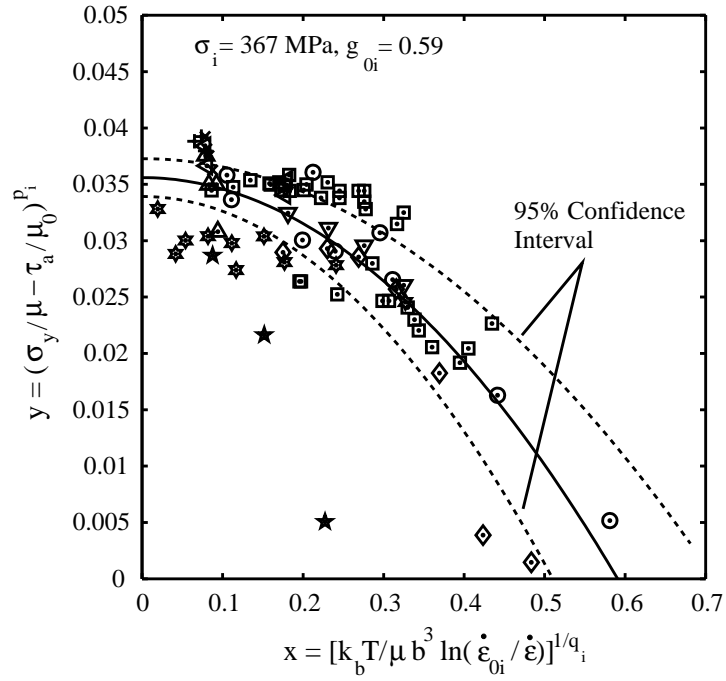
FIGURE 1. Fisher plot used to determine σ_i and g_{0i} for 6061-T6 aluminum alloy. The solid line shows the model fit to the data. The dotted lines show the range of the model for a confidence level of 95%. The symbols represent experimental data. The sources of the experimental data are: $\circ$: [45], $\square$: [46, 47], $\triangledown$: [48], $\star$: [23], $\triangle$: [49], $\diamond$: [50], $\times$: [51], $*$: [42], $\triangleleft$: [52, 53], $+$: [54, 55]
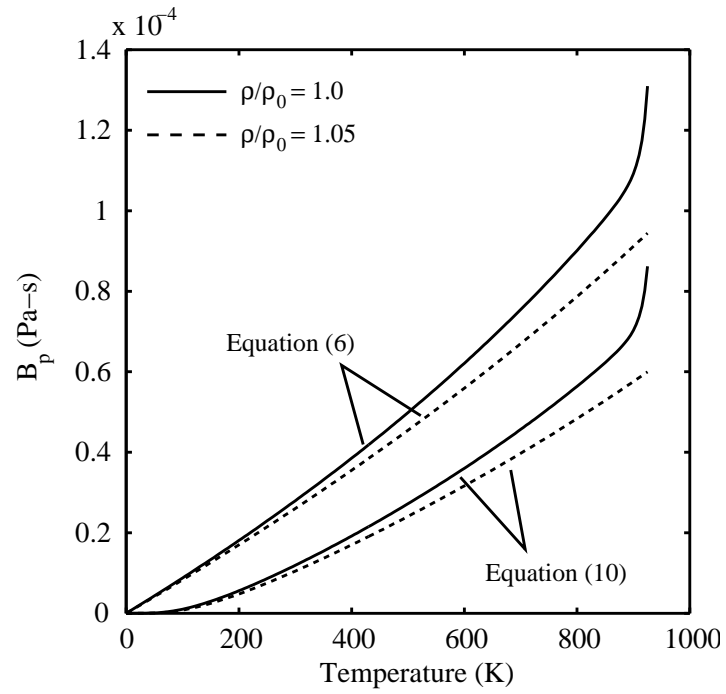
FIGURE 2. Phonon drag coefficient (B_p) as a function of temperature. The upper curve shows the prediction of the model in equation (6) and the lower curve shows the values predicted by the model in equation (10).
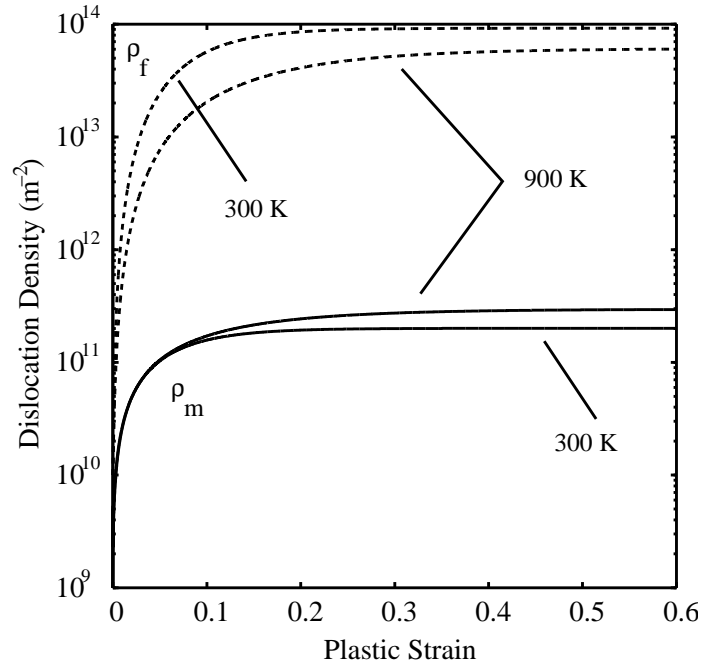
FIGURE 3. Evolution of dislocation density as a function of plastic strain and temperature. The solid curves show the evolution of ρ_m while the dotted curves show the evolution of ρ_f.
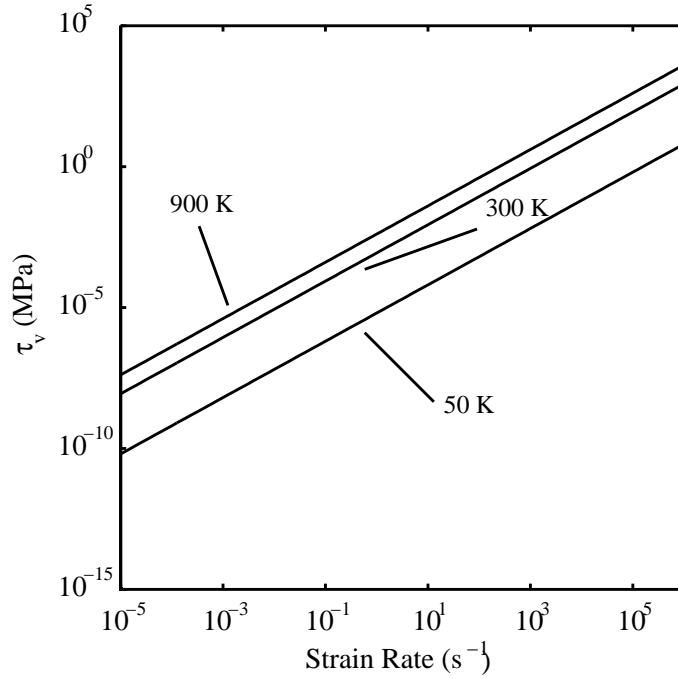
FIGURE 4. Variation of the viscous drag component of the flow stress of 6061-T6 aluminum with strain rate and temperature for a plastic strain of 0.2.

FIGURE 5. Fisher plot used to determine σ_{0es} and g_{0es} for 6061-T6 aluminum alloy. The solid line shows the model fit to the data. The dotted lines show the range of the model for a confidence level of 95%. The symbols represent experimental data. The sources of the experimental data are: $\circ$: [45], $\square$: [46, 47], ∇: [48], $\star$: [23], $\triangle$: [49], $\Diamond$: [50], $\times$: [51], $*$: [42], $+$: [52], $\triangleleft$: [53], $\triangleright$: [54, 55]
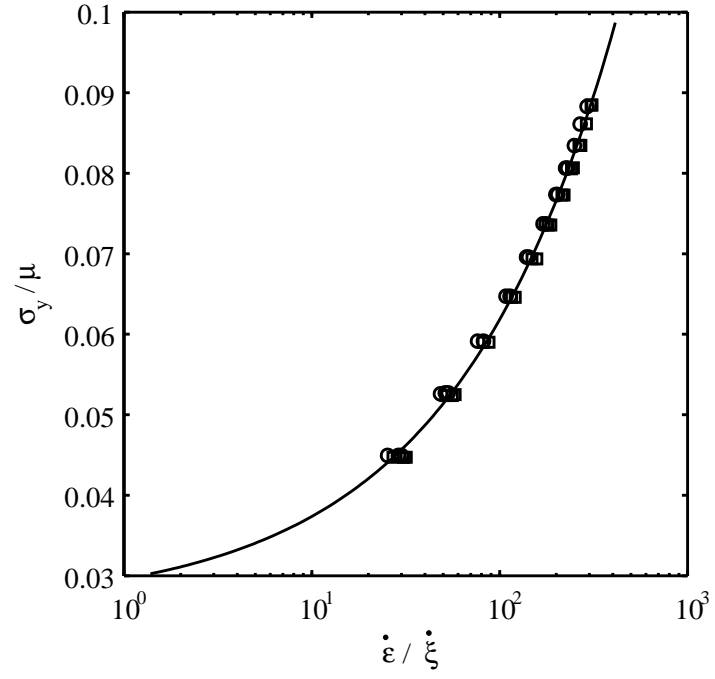
FIGURE 6. Comparison of the yield stress predicted by the overdriven shock model (equation 22) with experimental data. The solid line shows the predicted values. The circles show experimental data for 1100 aluminum alloy while the squares show experimental data for 2024 aluminum alloy.
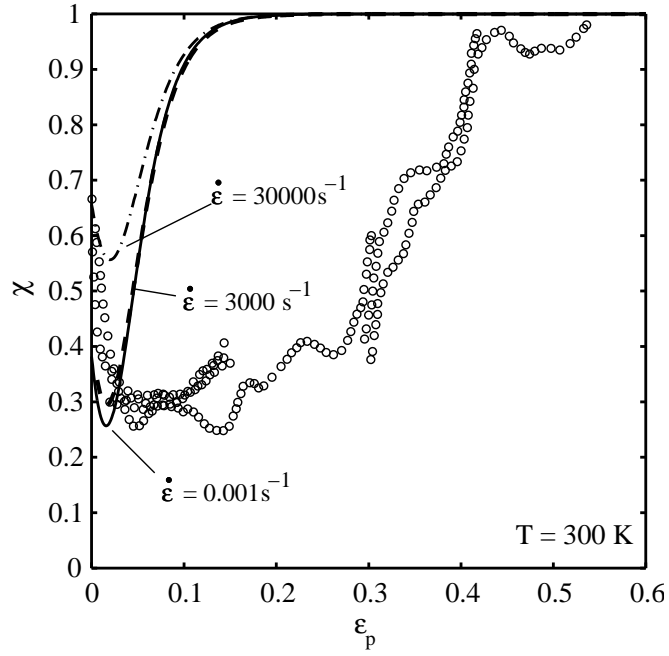
(a) T = 300 K.
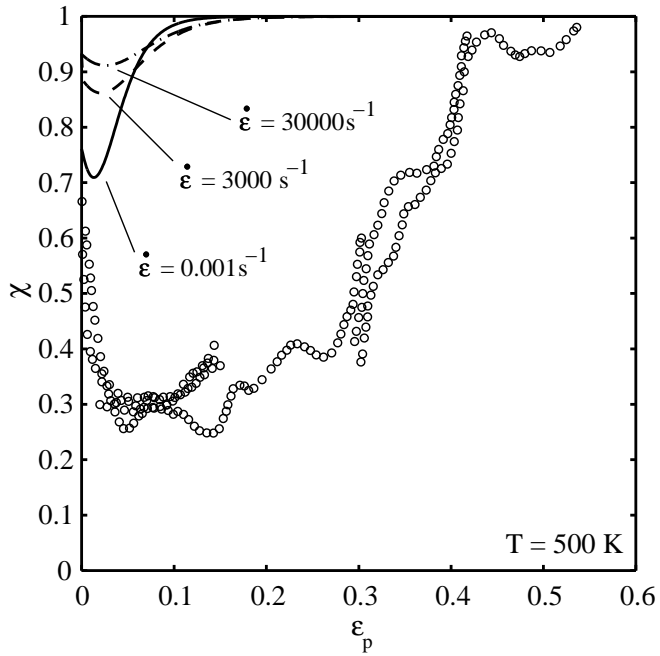
(b) T = 500 K.

FIGURE 7. Variation of the Taylor-Quinney coefficient (χ) with plastic strain and strain rate. The circles show experimental data for 2024-T3 aluminum alloy from [39] for a strain rate of 3000 s^{-1} and at 300 K. The solid lines represent predicted values for a strain rate of 0.001 s^{-1}. The dashed lines represent predicted values for a strain rate of 3000 s^{-1} and the dash-dot lines represent predictions for a strain rate of 30,000 s^{-1}.
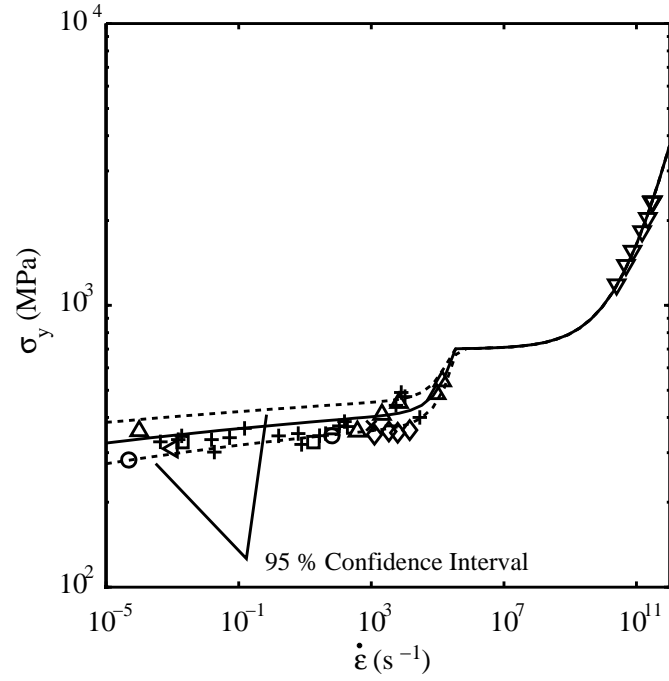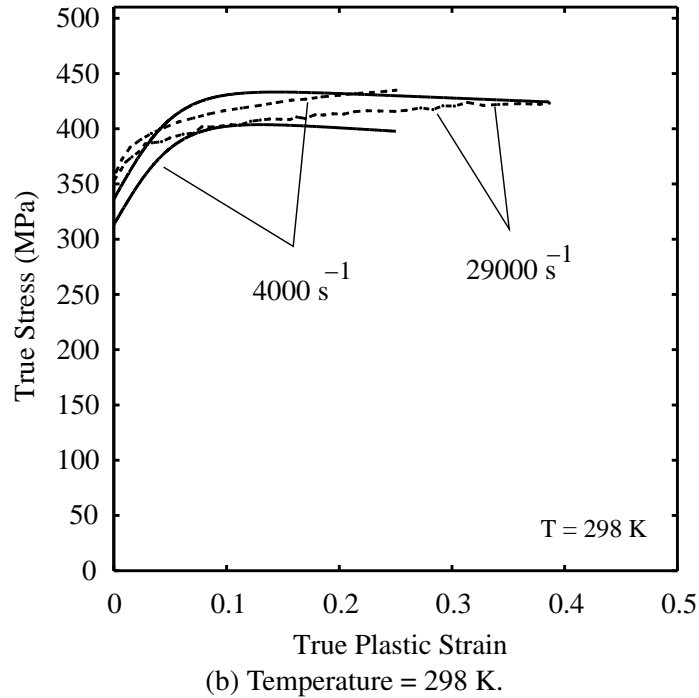
FIGURE 8. The flow stress of 6061-T6 aluminum alloy as a function of strain rate (at 298 K and a plastic strain of 0.2). The solid line shows the prediction of the extended MTS model. The dashed lines show the range of predicted flow stresses in the 95% confidence interval. The symbols represent experimental data. The sources of the experimental data are: $\circ$: [45], $\square$: [46, 47], $\triangledown$: [57], $\triangle$: [49], $\times$: [51], $\triangleleft$: [52], $+$: [54, 55], $\diamond$: [43]
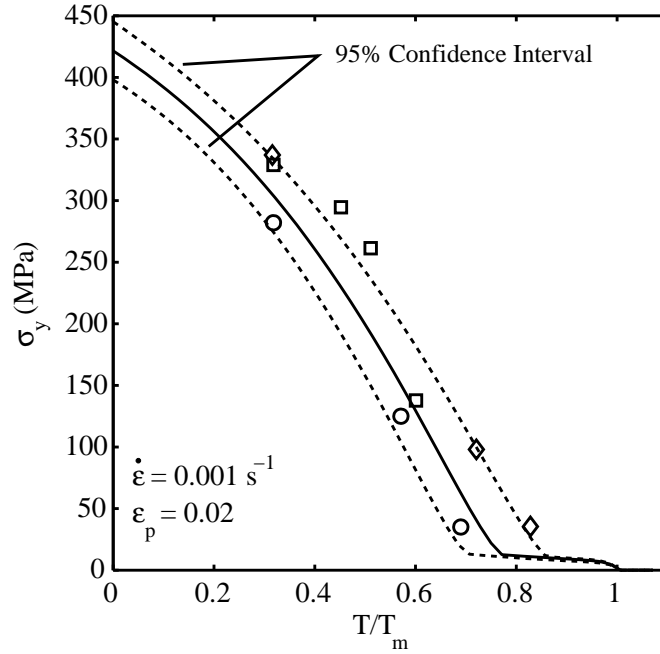
(a) Strain rate = 0.001 s^{-1} and plastic strain = 0.02.
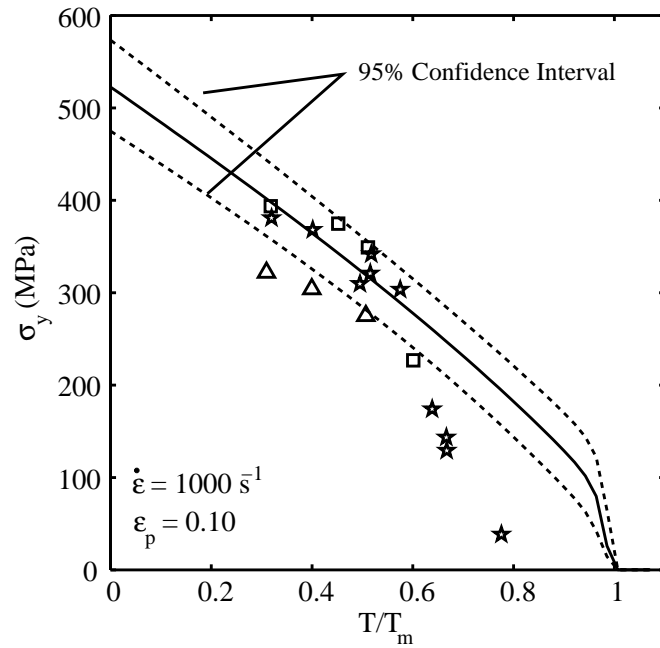
(b) Strain rate = 1000 s^{-1} and plastic strain = 0.1.

FIGURE 9. The flow stress of 6061-T6 aluminum alloy as a function of temperature. The solid lines show the prediction of the extended MTS model. The dashed lines show the range of values predicted if we use the low or high values of the parameters σ_i, g_{0i}, σ_{0es}, and g_{0es}. The symbols represent experimental data. The sources of the experimental data are: $\circ$: [45], $\square$: [46, 47], $\Diamond$: [60], $\star$: [23], $\triangle$: [42]
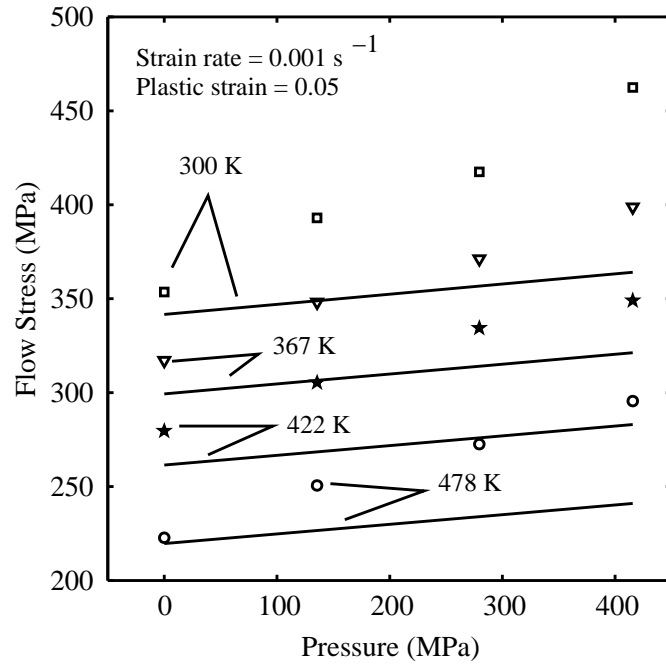
FIGURE 10. The flow stress of 6061-T6 aluminum alloy as a function of pressure for a strain rate of 0.001 s^{-1} and a plastic strain of 0.05. The solid lines show the predictions of the extended MTS model. The symbols represent experimental data from [48] at the following temperatures: range of values predicted if we use the low or high values of $\square$: 300 K, $\triangledown$: 367 K, $\star$: 422 K, and $\circ$: 478 K.

(a) Ambient pressure.

(b) Pressure = 276 MPa.
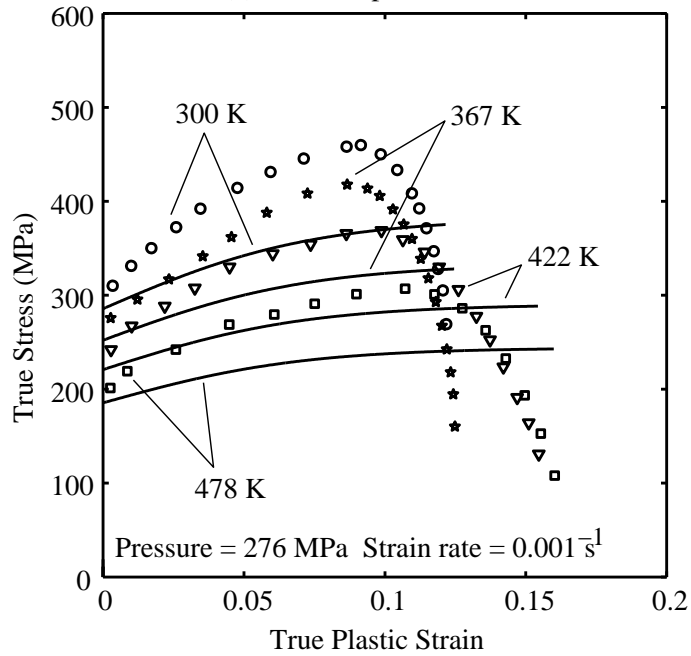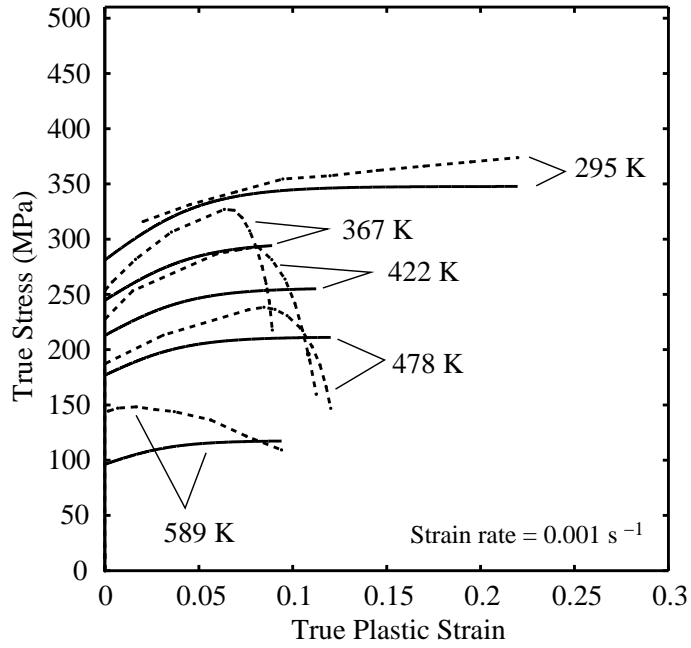
FIGURE 11. The flow stress of 6061-T6 aluminum alloy as a function of true plastic strain at a strain rate of 0.001 s^{-1}. The solid lines show the prediction of the extended MTS model. In part (a) of the figure the dashed lines represent the experimental data. In part (b) of the figure the symbols represent the experimental data. The data at 295 K are from [53]. The data at 300 K, 367 K, 422 K, and 478 K are from [48]. The data at 589 K are from [46, 47].

(a) Strain rate = 1000-2000 s^{-1}.

(b) Temperature = 298 K.
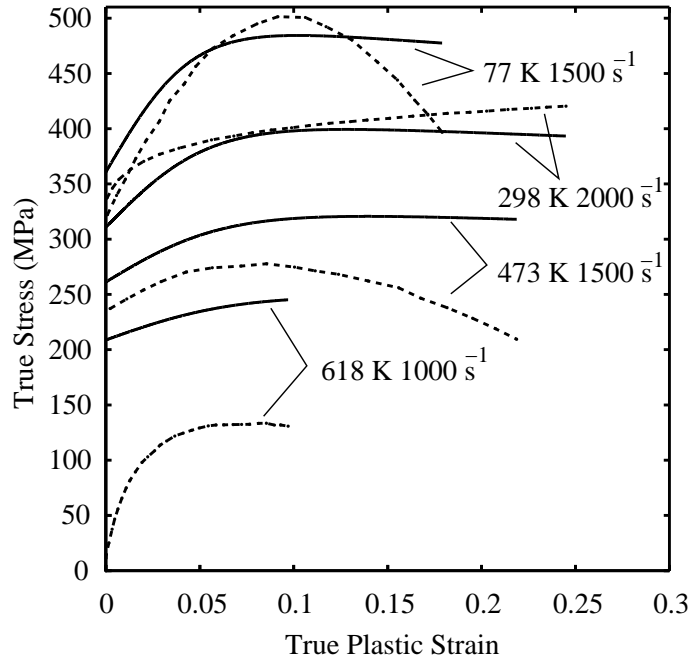
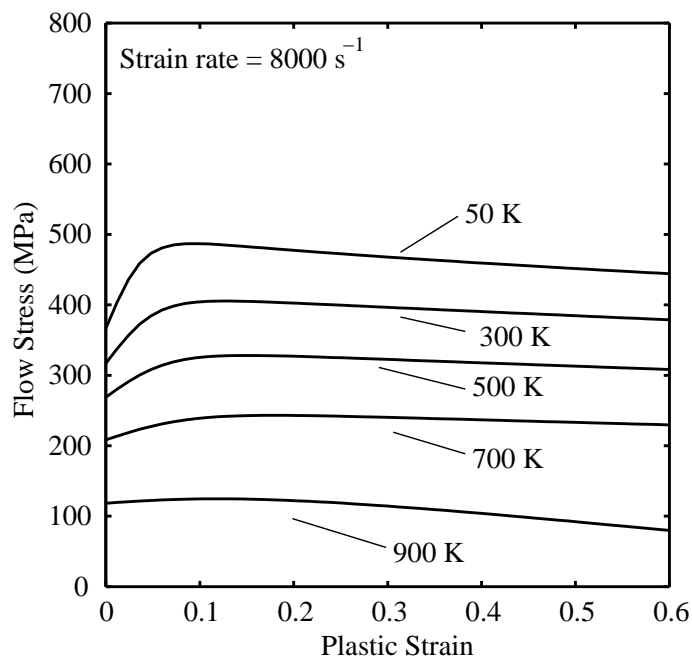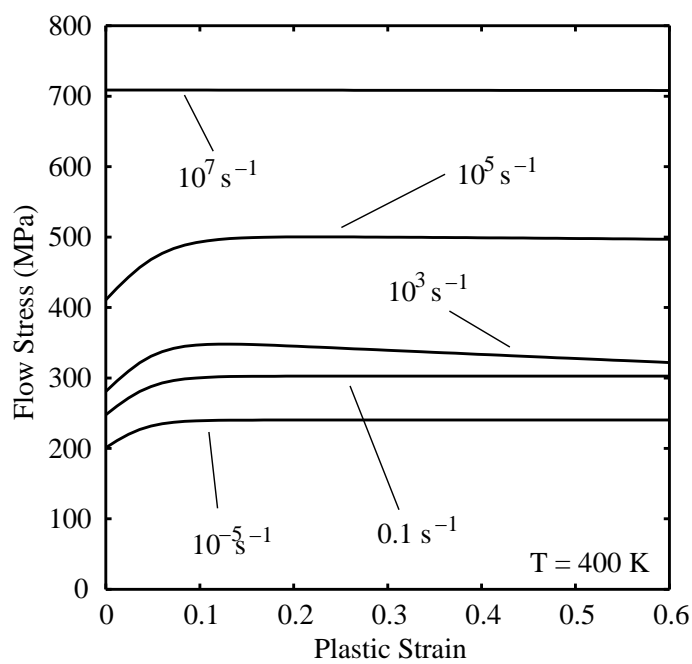FIGURE 12. The flow stress of 6061-T6 aluminum alloy as a function of plastic strain at moderately high strain rates. The solid lines show the prediction of the extended MTS model. The dashed lines represent the experimental data. The sources of the experimental data are: strain rate = 1000 s^{-1} from [23], strain rate = 1500 s^{-1} from [42], strain rates = 2000 s^{-1} and 4000 s^{-1} from [51], strain rate = 29000 s^{-1} from [55].
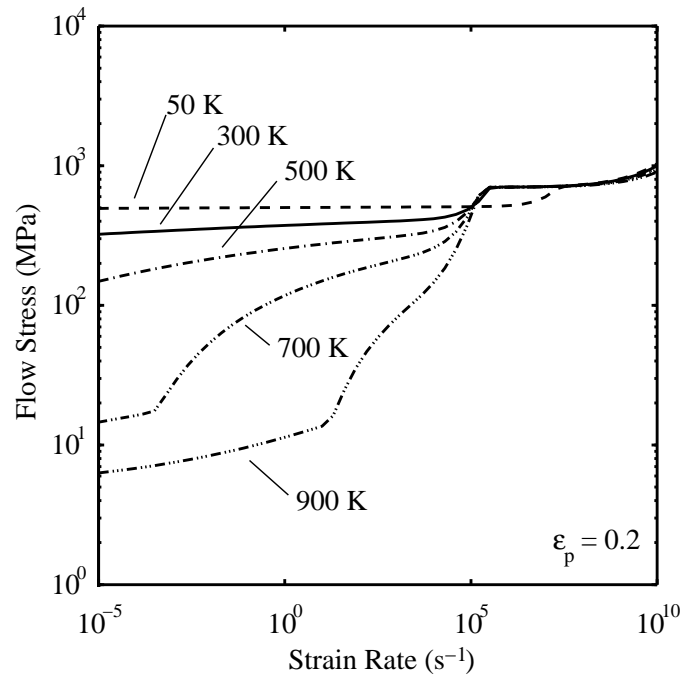
(a) Plastic Strain = 0.2.
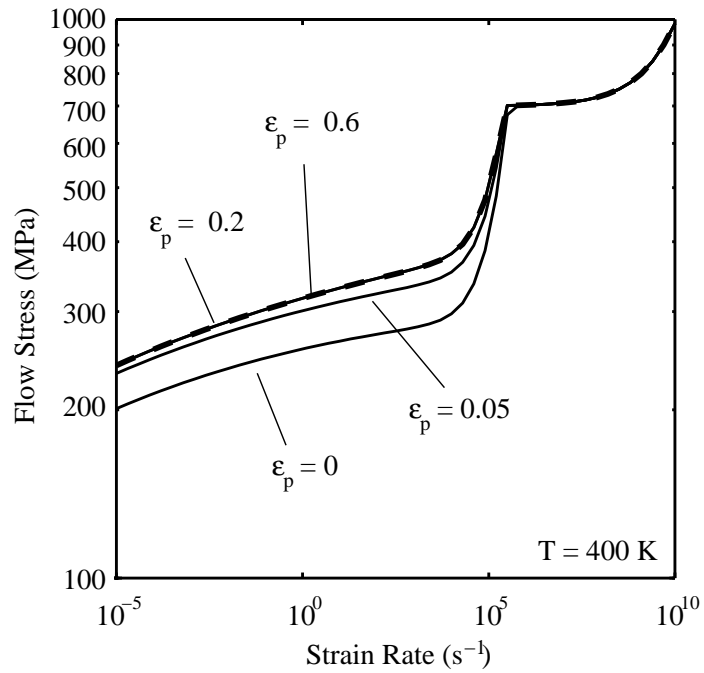
(b) Temperature = 400 K.

FIGURE 13. The predicted flow stress of 6061-T6 aluminum alloy as a function of strain rate.

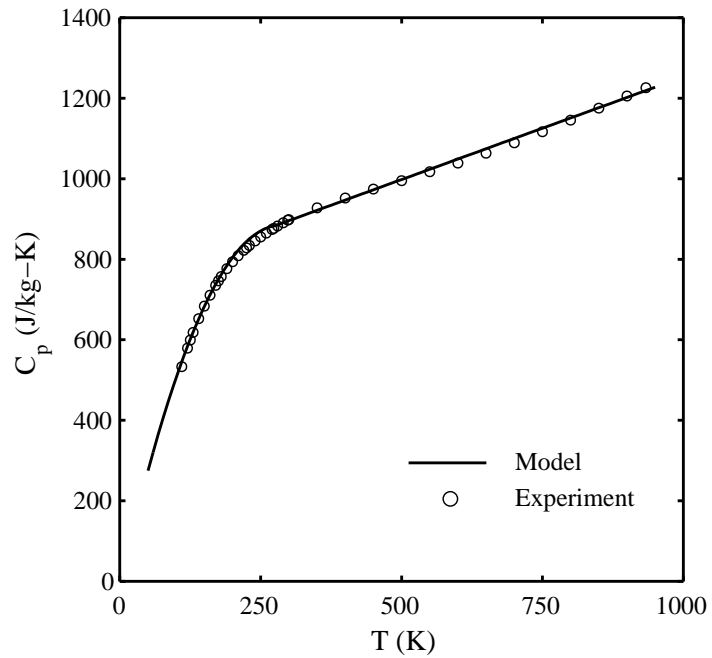(a) Plastic Strain = 0.2.

(b) Strain Rate = 8000 s^{-1}.
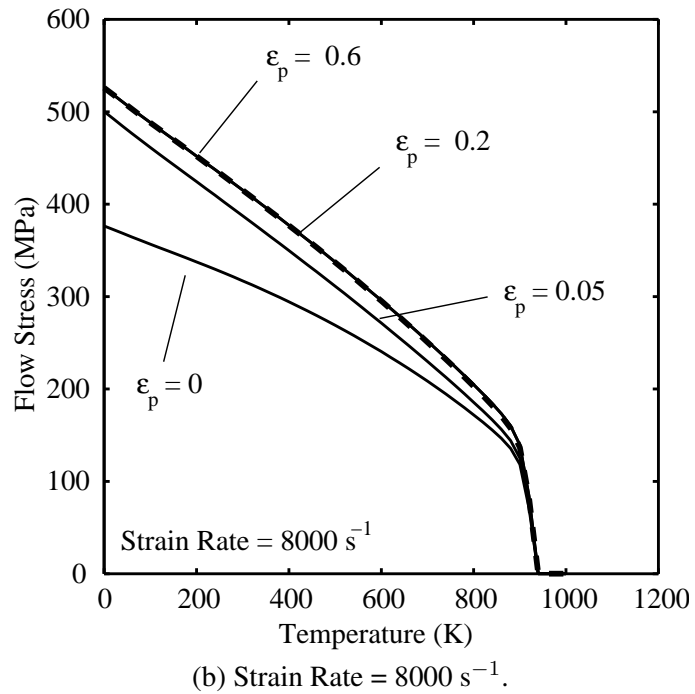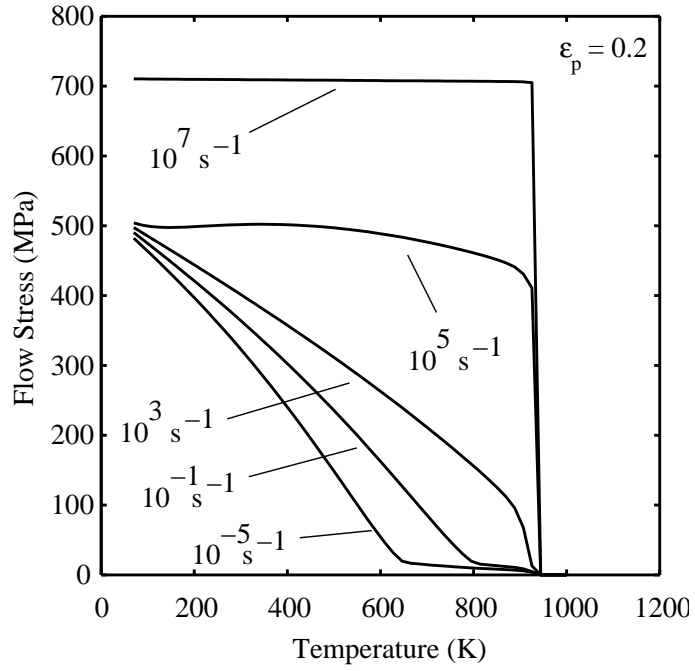
FIGURE 14. The predicted flow stress of 6061-T6 aluminum alloy as a function of temperature.

(a) Strain Rate = 8000 s^{-1}.

(b) Temperature = 400 K.

FIGURE 15. The predicted flow stress of 6061-T6 aluminum alloy as a function of plastic strain.

FIGURE 16. Specific heat of aluminum. The experimental data, shown as open circles, are from [64]. The solid line shows the prediction of the model in equation (31).
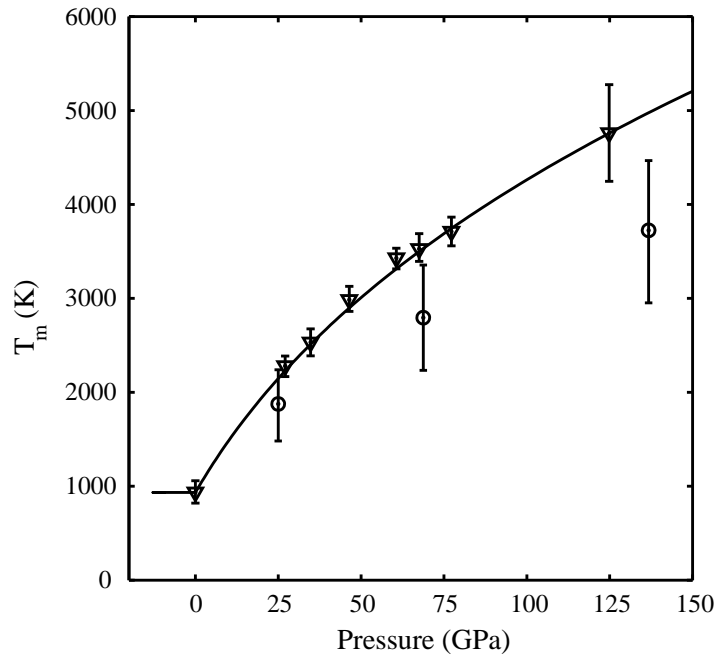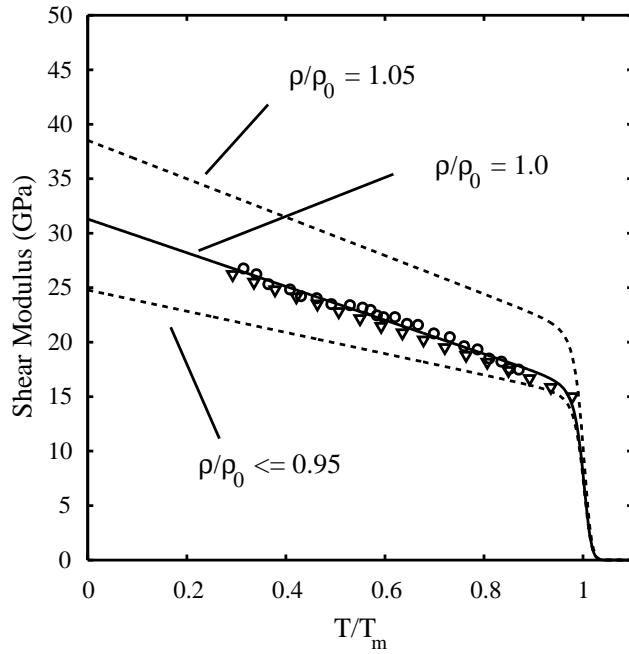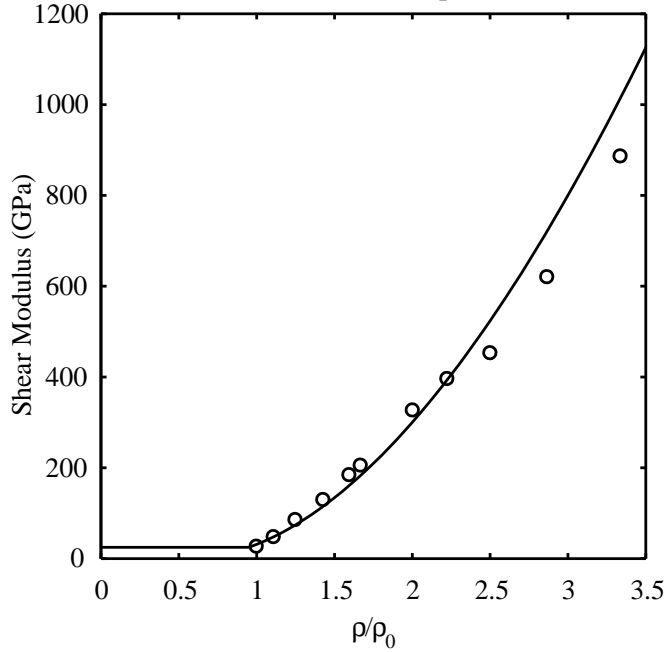

FIGURE 17. Melting temperature of aluminum. The triangles show experimental data from [68] and the circles show experimental data collected in [69]. The solid line shows the prediction of the model in equation (29).

(a) Shear modulus vs. temperature.

(b) Shear modulus vs. mass density at 0 K.

FIGURE 18. Shear modulus of 6061-T6 aluminum alloy. In part (a), the triangles show experimental data for pure aluminum from [72] and the circles show experimental data for 6061-T6 aluminum alloy from [50]. The solid line shows the prediction of the model in equation (26) at ambient pressure. The dotted lines show predicted shear moduli under hydrostatic tension and compression. In part (b), the circles show results from electronic structure calculations [33] and the solid line shows the prediction of our model.